

---

# EVALUATION OF ACOUSTIC EMISSION MONITORING OF EXISTING CONCRETE STRUCTURES

---

Master Thesis



OCTOBER 16, 2017  
DELFT UNIVERSITY OF TECHNOLOGY



# EVALUATION OF ACOUSTIC EMISSION MONITORING OF EXISTING CONCRETE STRUCTURES

Fengqiao Zhang





DELFT UNIVERSITY OF TECHNOLOGY  
NETHERLANDS ORGANIZATION FOR APPLIED SCIENTIFIC  
RESEARCH

**GRADUATION COMMITTEE**

**Chair holder:**

prof.dr.ir. D.A. Hordijk      Delft University of Technology

**Committee members:**

dr.ir. P.L. Pahlavan      Netherlands Organization for Applied  
Scientific Research

dr.ir. Y. Yang      Delft University of Technology

dr.ir. H.R. Schipper      Delft University of Technology



送给我的爸爸妈妈



## Abstract

An increasing number of existing structures are approaching the end of their technical service life. Therefore, monitoring these structures to get the information of their health condition, which is called structural health monitoring (SHM), is becoming more significant. In SHM, acoustic emission (AE) technique is one of the useful methods. AE is a phenomenon of wave radiation caused by the defect in structures, for example as a result of crack formation, etc.. By continuously recording and processing the signals emitted by the AE source, AE technique shows promising features in detection, localization and characterization of damage. This technique has been applied in many fields, such as steel structures, composite structures and concrete structures.

In dealing with existing concrete structures, cracks can influence the features of AE signals when they are on the way from the defect to the sensor. Therefore, it may challenge the commonly-used notion of AE monitoring. The influence of crack on AE monitoring has not been sufficiently investigated. More quantitative assessment on the crack influence on AE signals is believed to be valuable for the evaluation of accuracy and reliability of AE monitoring of existing concrete structures.

In this research, the influence of crack on AE signals has been studied quantitatively. Experiments on cracks with different opening have been performed to support the formulation of the signals. To have an overall understanding of waves from the source to the receiver in a cracked concrete beam, experiments on coupling effect and wave propagation in concrete medium, which will influence the recorded signals, are also carried out. The results are then used as inputs for an analytical study on source localization influenced by a crack. A three-dimensional (3D) triangulation technique has been used for source localization on a modeled cracked concrete beam. Localization error can therefore be estimated for AE sources in the presence of existing cracks. Furthermore, the influence of a crack on the amplitude of AE signals has been discussed. With the demonstrated crack-induced errors and attenuations ranges, the results can provide insights to the accuracy and reliability of AE monitoring in practical situations.



# Nomenclature

## Abbreviations

$nD$	$n$ -dimensional ( $n=1,2,3$ )
AE	Acoustic emission
RC	Reinforced concrete
SEM	Spectral finite element model
SHM	Structural health monitoring

## Greek letters

$\alpha$	Material attenuation coefficient
$\nu$	Poisson's ratio
$\rho$	Density
$\theta$	Angle between wave travel direction and crack surface normal direction

## Roman letters

$a_i$	Amplitude of signal $i$
$a_i^*$	Normalized amplitude of signal $i$
$A_i$	Peak amplitude of signal $i$
$c_p$	P-wave speed
$c_R$	R-wave speed
$c_S$	S-wave speed
$c_x$	Wave speed in orthogonal direction to the crack direction
$c_y$	Wave speed in parallel direction to the crack direction
$D$	Coupling effect function
$e_i$	Localization error in $i$ direction, $i = x, y, z$
$E$	Young's modulus
$f$	Wave frequency
$MA$	Material attenuation
$P$	Received signal
$r$	Source sphere radius
$S$	Source signal
$SL_b$	Spread loss of body waves
$SL_s$	Spread loss of surface waves
$t_i$	Arrival time at sensor $i$
$t_0$	Source time
$T_{cr}$	Transmission function of a crack
$w$	Crack width
$W$	Transfer function in concrete medium

$x$	Travel distance
$\mathbf{n}_0$	Normal direction of crack plane
$\mathbf{x}_G$	Location of grid point
$\mathbf{x}_s$	Source location
$\mathbf{x}_s^*$	Calculated source location
$\mathbf{x}_{R,i}$	Location of sensor $i$

## Preface

My master thesis lasted for around 1 year in the 23<sup>rd</sup> year of my life. I appreciate this experience a lot for the knowledge I learned, the life I discovered, and the people I met. Looking back to this period, I could feel my progress from a girl who hardly knew anything about structural health monitoring, who was very shy in expressing, and who was not confident enough. It is the people who supported me that made me find and develop myself.

Firstly, I would like to thank my daily supervisors Pooria Pahlavan and Yuguang Yang.

Pooria Pahlavan: He led me into the field of structural health monitoring. Thanks for his patience and tolerance on my slowness with almost zero background in this field. He also told me lessons on life, e.g. professional attitudes, communications and making decisions. He gave me many precious opportunities, for example, the chance of attending a conference and making public speech, the chance of knowing other professionals, and the information about further development like the possible PhD opportunities. I will always remember his help and support and always feel indebted to him.

Yuguang Yang: He was my teacher on concrete cracks before this master thesis. He also led me to know about the acoustic emission techniques on structural monitoring. I could still remember the day I came to him for the chance of master thesis. In the beginning I was very shy. It was his support, advice and encouragement that helped me grow up and build my confidence. He taught me in patience how to design a test, how to write thesis, etc.. His creative and critical opinions encouraged me to get better results. Besides the technical supervisor, he was also like a good friend. His kindness made the life warmer.

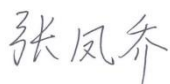
I would also like to thank other committee members. I would like to thank Dick Hordijk for his substantial support and encouragement. I would like to thank Roel Schipper for the inspiring discussions during the meeting.

Thanks also go to my colleagues in the lab. I want to thank the technician: Albert for his great instructions and help on the test performing. I want to thank my partner: Chengcheng for her kindness and tolerance when we collaborated in the tests. I also want to thank people in TU Delft in the lunch club for the enjoyable time. I would also thank my colleagues in TNO for their kind instructions on the work and future development.

I will also give my thanks to my friends Jian Jiao, Qiunan Tan, Jiaying Fang, Jiayi Wang, Jinxuan He and Zhekang Huang. Their accompany and support made my life in Netherlands more comfortable and colorful. I will always treasure our friendships.

A special and important acknowledgement is for my boyfriend Lichao Wu. I would like to thank all the accompany, care and support he gave me. My life with him was full of happiness.

The last but the most important thank is for my father and mother. Their great love made what I am. I will dedicate this work to them with my greatest gratitude.



Fengqiao Zhang

Oct. 6, 2017

Delft, the Netherlands



# Contents

Abstract.....	i
Nomenclature.....	iii
Preface.....	v
1 Introduction .....	1
1.1 Acoustic emission (AE) monitoring of existing concrete structures.....	1
1.2 Two AE monitoring approaches .....	1
1.3 Source Localization.....	2
1.4 Outline of the thesis.....	3
2 Elastic Wave Propagation in Concrete Structures .....	5
2.1 Body waves propagation in infinite medium .....	5
2.2 Surface wave propagation on an infinite surface .....	6
2.3 Wave Propagation in cracked concrete beam .....	6
3 Parameter-based Study on the Elastic Wave Propagation and evaluation of parameters ..	9
3.1 Simulations.....	10
3.2 Evaluation of parameters in parametric study.....	12
3.3 Concluding remarks .....	18
4 Experiments .....	21
4.1 Sensor coupling effect.....	21
4.2 Transfer function in concrete medium .....	23
4.3 Transmission function of cracks with different crack widths .....	27
4.4 Anisotropic transmission function of several cracks.....	31
4.5 Concluding remarks .....	33
5 Source Localization .....	35
5.1 Localization methods .....	35
5.1.1 Analytical solution.....	35
5.1.2 Grid search method.....	36
5.1.3 Localization error.....	37
5.2 Analytical study.....	37
5.3 Results .....	39
5.3.1 Accuracy of localization for partially-closed cracks .....	39
5.3.2 Reliability of localization for partially-closed cracks.....	51
5.3.3 Accuracy of localization for open cracks.....	52
5.3.4 Reliability of localization for open cracks .....	54

5.4	Concluding remarks .....	54
6	Conclusions and recommendations .....	55
6.1	Conclusions .....	55
6.2	Recommendations .....	55
A.	Appendix: Elastic vector wave equations.....	57
B.	Appendix: Geometric spread loss.....	61
	Reference .....	63

# 1 Introduction

## 1.1 Acoustic emission (AE) monitoring of existing concrete structures

The maintenance of the existing concrete structures is getting more significant in the consideration of safety, environment and economy [1]. Structural health monitoring (SHM), which is a process to implement a damage detection and characterization for structures, can offer an evaluation of the integrity of existing concrete structures in real time [2-4]. Structural health monitoring may reduce the operational costs and prevent unnecessary maintenance by replacing scheduled maintenance with as-needed maintenance [5].

Acoustic emission (AE) technique is one of the SHM methods. AE is considered as a passive phenomenon and mostly related to a damaging process in the load history [6]. The released energy excites elastic waves which are recorded by the sensors and converted to electrical signals. By continuously recording and processing the signals, AE technique can provide insight into fracturing processes in structures remotely and without interrupting its function and integrity [7, 8]. One of the promising features of AE technique is that the damage process can be tested during the whole load history without disturbing the loading [6].

The application of AE technique started from detecting fatigue cracks in metallic structures [9, 10]. However, the AE monitoring of concrete structures is more challenging due to the complexity of the concrete material. The complexity can be ascribed to the heterogenous and anisotropic property of the material, such as the scattering by the aggregates and the presence of cracks. Studies of AE monitoring in concrete structures include many aspects, such as the localization of the source [11-13], the characterization of damage [14, 15], AE tomography [8, 16], and decision making in load testing [17, 18]. Figure 1.1 shows the AE monitoring on a concrete bridge in Netherland.



*Figure 1.1: AE tests on Ruytenschildt bridge*

## 1.2 Two AE monitoring approaches

There are two commonly-used approaches of AE monitoring in regard to data acquisition and signal processing. One is signal-based method and the other is parameter-based method [6].

In the parameter-based method, the stored data are some parameters extracted from the waveform, for example, the counts number, the peak amplitude, etc.. This approach can be efficient and economic especially for monitoring large structures over long period of time, but also may compromise accuracy by only using a few parameters to represent the whole waveform.

In the signal-based method, the whole waveform is recorded and stored by the acquisition system for the further processing and interpretation. It is time consuming and costly for data management and processing, but more accurate by providing full information of the signals.

Since parameter-based method is widely used currently, in this thesis, an evaluation of this approach in the analysis of AE signals is performed. Firstly, it is evaluated based on a numerical simulation of wave propagation in a concrete medium from a point source. The conclusions are further evaluated using the acquired data from real tests.

### 1.3 Source Localization

In AE monitoring, one of the main objectives is source localization. It aims at estimating the position of the source, which can be the crack opening or closing in concrete structures. The recorded signals are processed with source localization algorithms to determine the location of the source. Such algorithms are usually based on the traditional triangulation technique [11], which assumes a constant wave speed in the medium. In this method, by knowing the arrival times of the signals and wave speed can we calculate where the source is. An example of source localization in a four-point bending test [19] is shown in Figure 1.2. In the top figure in Figure 1.2, sensors which were installed on the surface of the beam are shown as the ‘plus’ marks, and the cracks are marked as cr1 – cr5. Localization results are shown as black dots in the bottom figure in Figure 1.2. It can be found that only cr3 and cr5 of the five cracks can be localized with an acceptable error. The deficiency that only a limit number of detected events can be localized accurately may due to the heterogenous property of concrete medium, or more importantly the presence of cracks.

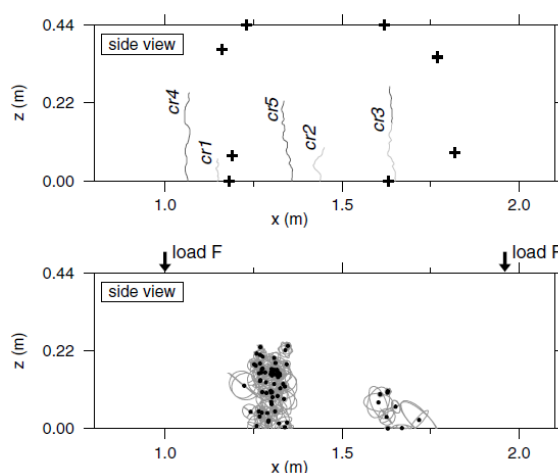


Figure 1.2: Sensor distribution with crack pattern (top) and localization results (bottom) [19]

To deal with these shortcomings in the commonly-used source localization method, further developments have been explored. Gollob considered the heterogenous property of the material with different wave speeds in 2017 [20]. It applied multi-segment wave propagation path based

on a heterogenous velocity model in the concrete. Another assessment on the influence of an open crack on source localization was also studied by Tsangouri et al, 2016 [21]. It analyzed the localization accuracy with respect to the developing of an open crack.

It is not sufficient for the evaluation of AE source localization in the existing concrete structures that only the influence of an open crack is studied. Depending on the loading condition, the entailing cracks could be relaxed due to the unloading of the structure globally or locally. In this thesis, those relaxed cracks due to the unloading are defined as partially-closed cracks. A partially-closed crack may have a different influence on the wave propagation and thus a different result of source localization. More AE sources may not lead to more recorded signals due to the high attenuation of the signals caused by the partially-closed cracks. The influence of a partially-closed crack remains to be researched quantitatively, thus it is the subject of this thesis.

## **1.4 Outline of the thesis**

This thesis mainly contributes to the evaluation of AE monitoring of existing concrete structures, by a combination of experimental study and analytical study. A brief description to the organization of the thesis is provided below.

In Chapter 2, background knowledge on the elastic wave propagation in un-cracked concrete structures is reviewed. The concrete medium is assumed to be homogeneous and isotropic. For cracked concrete structures, two possible wave propagation paths are discussed, in consideration of different status of cracks.

In Chapter 3, the elastic wave propagation in concrete medium is studied using parameter-based method. Some commonly-used parameters are evaluated. The study is based on a numerical simulation of wave propagation in the concrete medium and measurement phenomena.

Chapter 4 is dedicated to exploring the wave propagation experimentally. Measurements on the coupling effect, wave propagation in concrete medium, and the influence of partially-closed cracks with different surface widths are performed. The results of the tests provide the basis for the later analytical study on source localization.

The objective of Chapter 5 is to study the influence of cracks on the AE source localization. In the beginning, a standard three-dimensional (3D) triangulation technique for source localization is implemented. Afterwards, the experimentally-obtained influence of a partially-closed crack is included in the localization algorithm. Subsequently, an analytical study on the accuracy and reliability of source localization on a modeled cracked concrete beam is provided. The situations of an open crack and a partially-closed crack are both considered. The comparable results offer new insights for the evaluation of AE monitoring of existing concrete structures.



## 2 Elastic Wave Propagation in Concrete Structures

A damaging process in concrete structures can suddenly release energy and excite elastic waves. Similar to the seismic waves [22], two basic types of elastic waves can be generated by an AE source, i.e. body waves and surface waves. These waves will propagate in concrete structures and be detected by the AE sensors. The acquired signals are generally influenced by the wave propagation in the medium. Therefore, background of elastic wave propagation in concrete is important for the interpretation of AE signals, especially in consideration of the influence of existing cracks.

### 2.1 Body waves propagation in infinite medium

Body waves travel through the interior of concrete structures. Different particle motions can result in two types of body waves: primary waves (P-waves) and secondary waves (S-waves). P-waves are also called as longitudinal waves since the particle movement is along the direction of propagation. S-waves are also called as transverse waves in which particle motions are transverse to the direction of propagation.

If the wavelength is sufficiently large compared to the size of the aggregates, the velocities  $c_p$  and  $c_s$  of P-waves and S-waves, respectively, can be theoretically calculated as:

$$c_p = \sqrt{\frac{E(1-\nu)}{\rho(1+\nu)(1-2\nu)}} \quad (2.1)$$

and

$$c_s = \sqrt{\frac{E}{2\rho(1+\nu)}} \quad (2.2)$$

where,  $E$  is the Young's modulus in  $\text{N/mm}^2$ ,  $\nu$  is the dynamic Poisson's ratio, and  $\rho$  is the density in  $\text{kg/m}^3$ .

The derivation of the wave velocities can be found in Appendix A.

For a concrete specimen with the Young's modulus of  $31000 \text{ N/mm}^2$ , the dynamic Poisson's ratio of 0.25, and the density of  $2324 \text{ kg/m}^3$ , the speeds of P-waves and S-waves are calculated as  $4000 \text{ m/s}$  and  $2310 \text{ m/s}$ , respectively.

The reduction of the amplitude of the elastic waves, which can be referred as attenuation, contains geometric spread loss and material attenuation. Body waves propagate spherically from the source in space. Therefore, the geometric spread loss follows the spherical spread rule and can be calculated in decibels as:

$$SL_b = 20 \log_{10} \left( \frac{r}{x} \right) \quad (2.3)$$

where  $r$  is the source sphere radius in m, and  $x$  is the travel distance to the source in m.

The geometric spread loss of body wave is derived in Appendix B.

Material attenuation highly depends on the propagation medium and frequency [23]. Material attenuation in decibels can be expressed as:

$$MA = \alpha \cdot x \cdot f \quad (2.4)$$

where,  $\alpha$  is the material attenuation coefficient in dB/(m·MHz),  $x$  is the travel distance to the source in m,  $f$  is the wave frequency in MHz.

## 2.2 Surface wave propagation on an infinite surface

Surface wave travel along the surface in two dimensions. In concrete structures, the surface waves are mainly Rayleigh waves, in which particle motion can be parallel and perpendicular to the travel direction. Surface waves travel more slowly than body waves at an approximated speed [24] of:

$$c_R = \frac{0.862 + 1.14\nu}{1 + \nu} c_S \quad (2.5)$$

where  $\nu$  is the dynamic Poisson's ratio, and  $c_S$  is the velocity of S-waves.

For the same concrete specimen mentioned in the previous section, the theoretical speed of the surface waves is 2124 m/s.

The geometric spread loss of surface follows the cylindrical spread rule. The amplitude of surface waves radiated from a point source decays as:

$$SL_s = 20 \log_{10} \left( \sqrt{\frac{r}{x}} \right) \quad (2.6)$$

where,  $r$  is the source sphere radius in m,  $x$  is the travel distance to the source in m.

The derivation of the geometric spread loss of surface waves can be found in Appendix B.

From the equations above, over the same distance, surface wave propagates slower and with less attenuation compared to body wave.

## 2.3 Wave Propagation in cracked concrete beam

In the presence of existing cracks in a concrete structure, the emitted AE signals can experience extraordinary complications on their way from the source to the sensors attached to the structure surface. In general, waves may propagate in two possible ways when facing a crack depending on the status of the crack. For a fully-open crack, the waves will propagate on a tip-diffracted travel path [21]. It is schematically shown by Figure 2.1. The red dot indicates the assumed source. The blue arrows show the shortest wave propagation path. A general assumption is that the tip of a fully-opened crack changes the propagation direction without causing attenuation. Along the wave propagation path, the signals can be affected by the source pulse, wave transfer function in the concrete medium and the sensor coupling. In the case that

only one fully-open crack exists between the source and the receiver, as shown in Figure 2.1, the received signal can be described in frequency domain as:

$$P(f) = D(f) \cdot W(d, f) \cdot S(f) \quad (2.7)$$

where,  $f$  is the frequency,  $d$  is the total travel distance, i.e.  $d = d_1 + d_2$  (see Figure 2.1),  $P$  is the received signal,  $D$  is the coupling effect function,  $W$  is the transfer function in the concrete medium, and  $S$  is the source signal.

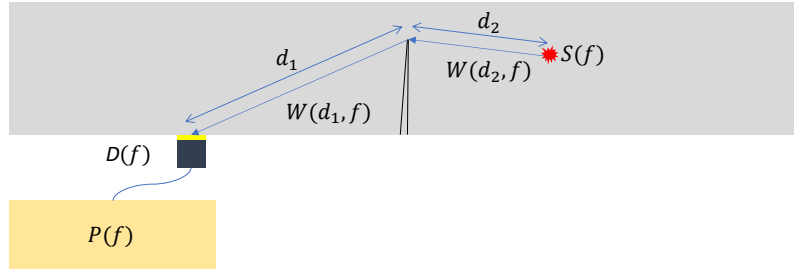


Figure 2.1: Tip-diffracted wave propagation path

Cracks can also be closed or partially closed, for example, when the cracks are under compressional stress. Waves may propagate through a partially-closed crack, as schematically shown in Figure 2.2, and cause additional influence on the detected signal. For the situation that a partially-closed crack exists between the source and the receiver, the received signal, therefore, can be described in the frequency domain as:

$$P(f) = D(f) \cdot T_{cr}(w, f) \cdot W(d, f) \cdot S(f) \quad (2.8)$$

where  $w$  is the opening of the crack on the surface, and  $T_{cr}$  is the transmission function of the crack.

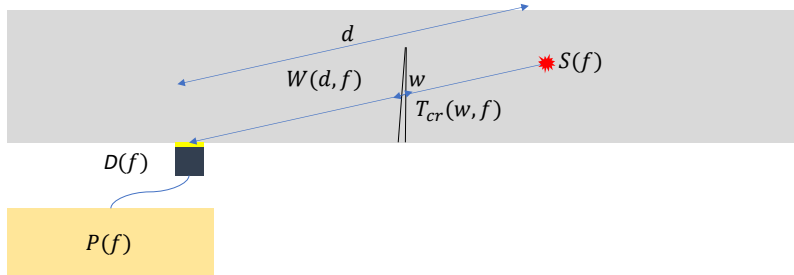


Figure 2.2: Direct wave propagation path

Based on the description of the influential factors of the recorded signals, some factors can be measured separately by controlling the other factors. For example, by comparing the two signals whose only difference is the travel path, i.e. travel through no crack or travel through a partially-closed crack, we can acquire the transmission influence. This approach is used in the design of the experiments in Chapter 4.



### 3 Parameter-based Study on the Elastic Wave Propagation and evaluation of parameters

Parameter-based method is introduced in Chapter 1. It has already been realized that the simply-calculated parameters may not be sufficiently accurate for distinguishing different waveforms. Therefore, an evaluation of some parameters extracted in the parameter-based methods is valuable.

In this chapter, a parameter-based study on the elastic wave propagation in concrete medium is carried out based on a simulated model. Since the whole waveform can also be acquired in the simulation, by comparing the signal-based results and parameter-based results, an evaluation of parameter-based method in the analysis of wave propagation in concrete medium can be performed.

The boundary condition of the simulation is that the responses are the nodal displacements, which means that the coupling effect is eliminated. Therefore, the evaluation doesn't consider the influence of couplant and sensor. If the chosen parameters could not give reliable information, it will not be reliable for the more complicated practical signals. If the evaluation of the parameters is positive, an additional verification using acquired data from real tests is added.

Parameters relate to the wave speed (i.e. arrival time), the wave energy (i.e. peak amplitude and energy) and the wave frequency (i.e. counts) are evaluated to check whether they can indicate the wave propagation. They are defined in RILEM [25] and illustrated in Figure 3.1. The dashed red line is the envelop of the waveform. The dashed black line in bold indicates the threshold level. The black circles show the counts. For the signal in Figure 3.1, the number of counts is four and the number of counts to peak is two.

- arrival time ( $t_{ar}$ ): the time when the amplitude first crosses the threshold level;
- peak amplitude ( $A_{max}$ ): largest amplitude in a waveform;
- duration time ( $T_d$ ): duration observed from the arrival time to the time when the amplitude decays to the level lower than the threshold;
- rise time ( $T_{rs}$ ): duration from the arrival time to the time of the peak amplitude;
- counts ( $C_d$ ): normally, AE counts imply number of times the signal amplitude exceeds the threshold;
- counts to peak ( $C_{rs}$ ): counts between the arrival time and the time of the peak amplitude;
- energy ( $E_d$ ): in principle, the area under the envelope of the waveform in range of duration time;
- rise energy ( $E_{rs}$ ): the area under envelope of the waveform in range of rise time.

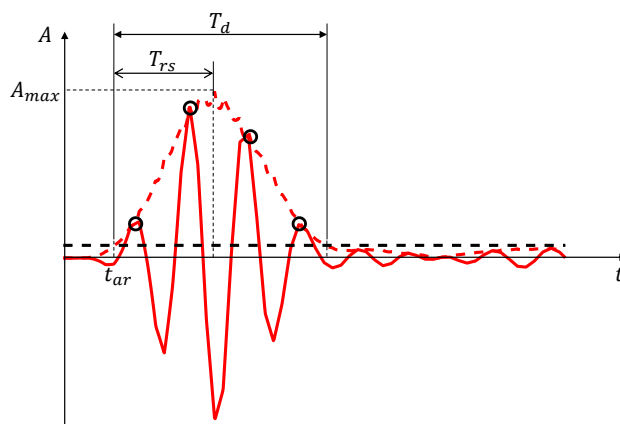


Figure 3.1: AE waveform parameters

### 3.1 Simulations

A two dimensional spectral finite element model (SEM) was implemented as [26]. The geometry was divided into elements with size of 2 mm × 2 mm. A beam section with length of 1.5 m and height of 0.5 m was modeled, with maximum aggregate size of 16 mm and 1% porosity, and without reinforcement. The locations, shapes and sizes of aggregates were randomly distributed and partly shown in Figure 3.2. Different element types for cement, aggregate, voids have been considered and assigned to each element based on the spatial location. The material properties of different element types are listed in Table 3.1. The Young’s modulus of aggregates had a ± 10% changing from the value shown in the table. They were randomly assigned to each aggregate.

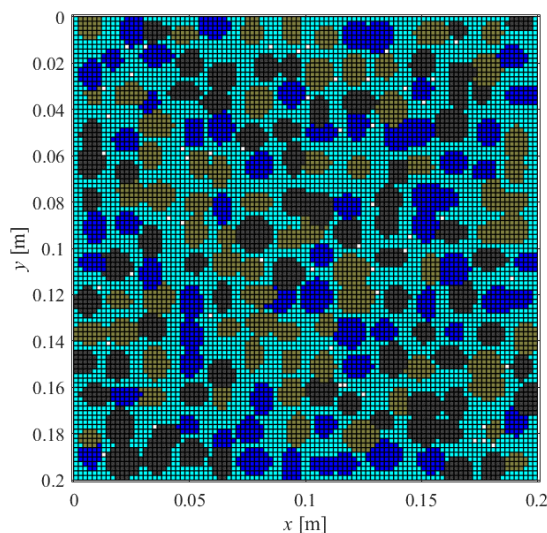


Figure 3.2: The finite element model of part of the section in 2D SEM

Table 3.1: Material properties of different element types

element type	density [kg/m <sup>3</sup> ]	Young’s modulus [N/mm <sup>2</sup> ]	Poisson’s ratio [-]
cement	2010	30000	0.2
aggregate	2650	60000	0.25

A five-cycle burst with center frequency of 60 kHz was generated and applied at position  $x = 0.32m$ ,  $y = 0.3m$  in  $y$ -direction. Seventeen receivers were arranged at the top with a spacing of 40 mm. The first receiver was right on top of the source. The locations of simulated source and receivers are shown in Figure 3.3 and the applied point load in time domain as well as frequency domain is shown in Figure 3.4.

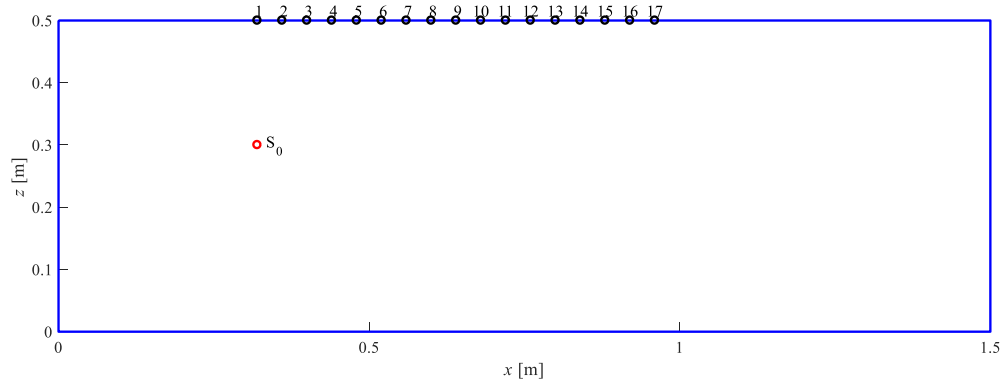


Figure 3.3: Beam configuration and locations of source and receivers

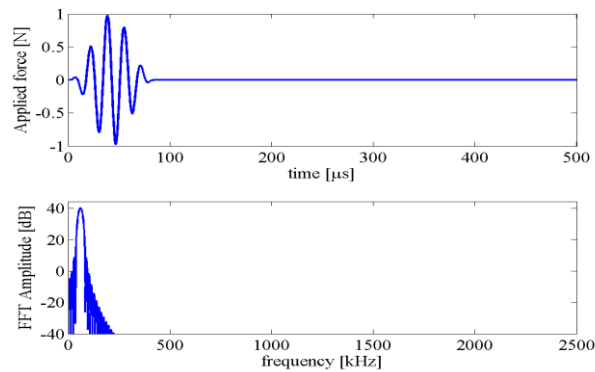


Figure 3.4: Applied point load as an AE source: (top) in the time domain and (bottom) in the frequency domain

Snapshots of the response at  $50 \mu s$  and  $150 \mu s$  are shown in Figure 3.5. It shows the response (displacement) in  $y$ -direction, which is the same direction as the applied point source. It can be observed that the P-waves which travel faster than S-waves have reached the top boundary at about  $50 \mu s$ . Complicated reflections at the top, bottom and left boundaries can be seen from the snapshot at  $150 \mu s$ . It should be noted that in a two dimensional simulation, the spread loss of body waves follows a cylindrical spreading model.

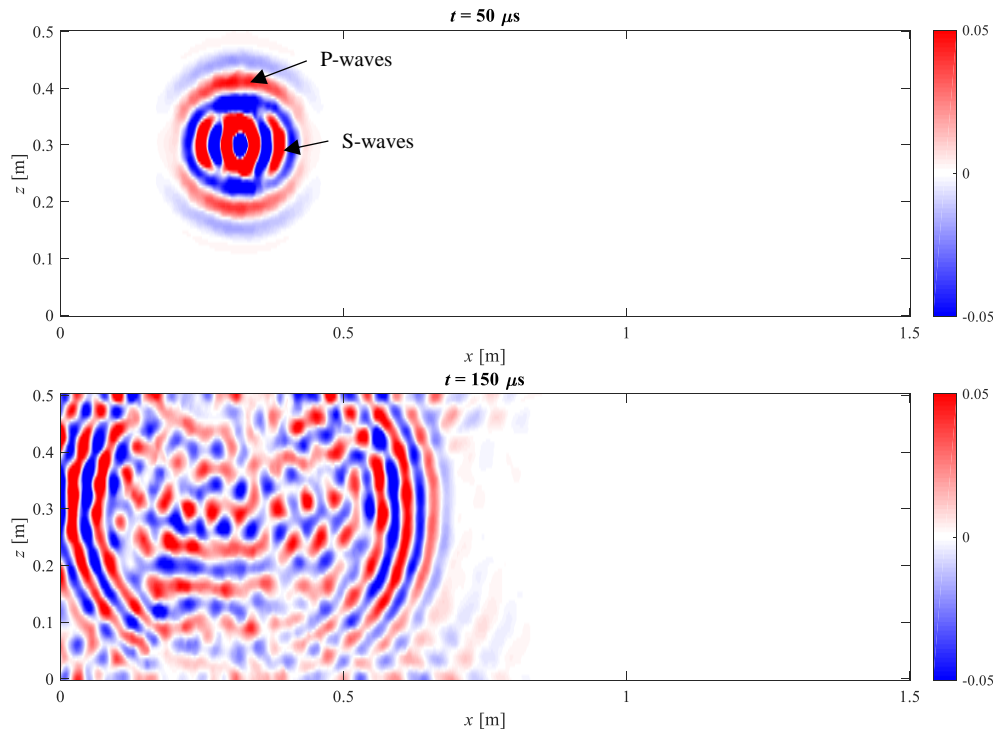


Figure 3.5: Snapshots of wave field at: (top)  $50 \mu s$ , (bottom)  $150 \mu s$

### 3.2 Evaluation of parameters in parametric study

Note that the responses at each sensor point is the displacement in  $y$ -direction. Therefore, the signals mentioned below represent the displacement responses. The amplitudes are in unit of  $m$ , and the energy is in unit of  $m \cdot \mu s$ .

Each signal was normalized by dividing the peak amplitude of itself, as shown in Figure 3.6. With the increase of the travel distance, the shape of the waveform got complicated by multiple wave modes and reflections. The signals were only recorded in a duration of  $500 \mu s$ , which contained 2502 sample points with a spacing of around  $0.2 \mu s$ .

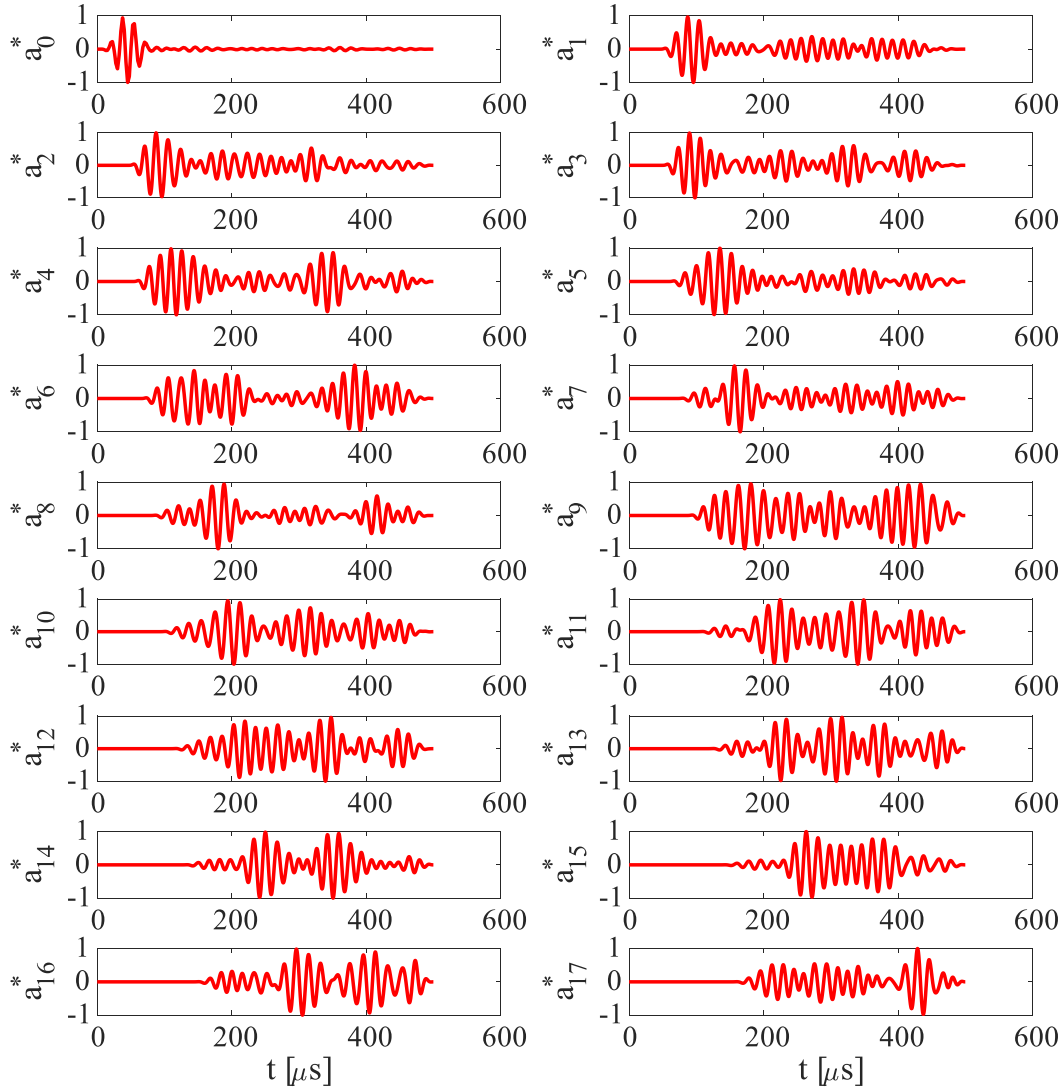


Figure 3.6: Normalized signals

A constant threshold was used for the extraction of parameters, since this applied in many practical cases. The peak amplitude (displacement in y-direction) of the source signal in this simulation was around  $1.62 \times 10^{-10}$  m and a constant threshold level of  $3.23 \times 10^{-13}$  m was set. The setting of threshold level was practical with a 54 dB drop from the source signal. For example, for a source with a peak amplitude of 90 dB, the threshold level was set to be 36 dB, which is what we normally use in the tests.

Parameters listed in the beginning of this chapter were extracted as definitions. The extraction of parameters from the signal in receiver 1 is shown in Figure 3.7, as an example. The red solid and dashed lines show the original signal and its Hilbert-transform envelope. The vertical back dashed lines indicate the range of duration, and the horizontal black dashed line shows the threshold level. The vertical and horizontal green dashed lines show the time when the signal reached the peak amplitude and the level of peak amplitude. The blue filled and hollow dots show the counts to peak and the total counts, respectively. In this signal, the distracted parameters are listed in Table 3.2. By comparing different values of one parameter in signals received at different locations, the performance of this parameter over travel distance can be evaluated.

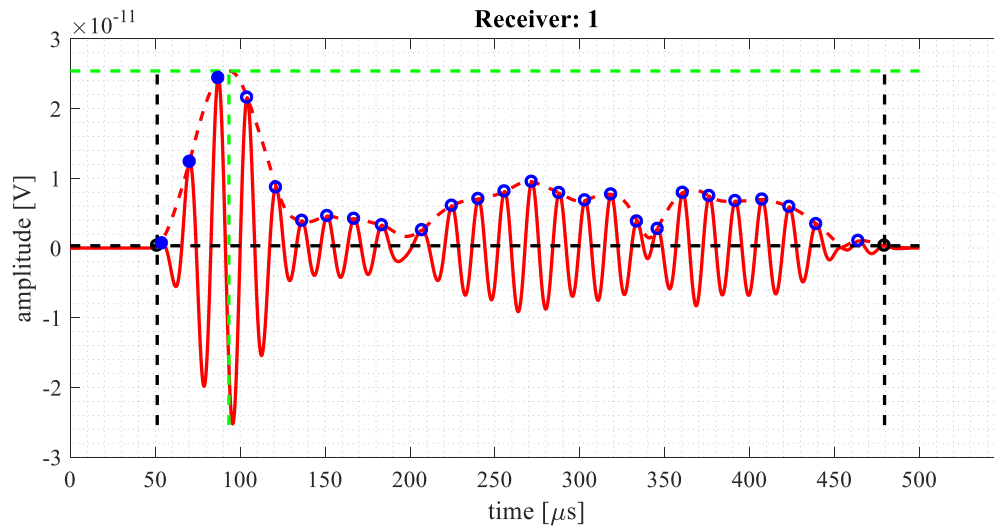


Figure 3.7: Extraction of parameters from signal in receiver 1

Table 3.2 Parameters of signal received in sensor 1

arrival time [ $\mu s$ ]	51.18
peak amplitude [ $m$ ]	$2.54 \times 10^{-11}$
duration time [ $\mu s$ ]	428.23
rise time [ $\mu s$ ]	42.18
counts [-]	26
counts to peak [-]	3
energy [ $m \cdot \mu s$ ]	$3 \times 10^{-9}$
rise energy [ $m \cdot \mu s$ ]	$5.85 \times 10^{-10}$

### 3.2.1.1 Arrival time

In the process of arrival time picking, some errors may occur in the processing of signals. For a signal which is attenuated more, a larger picking error can be generated. This is expected since the threshold level is constant while the signal-to-noise ratio decreased. The results of arrival time picking in signals 1 and 10 are compared in Figure 3.8. The red lines show the signals at receiver 1 with a larger peak amplitude, and the blue lines show the signals at receiver 10 with a smaller peak amplitude. The black dashed line shows the constant threshold level, with two hollow dots shown the picked arrival times of the two signals. As can be seen that the picked arrival time in the signal at receiver 10 was around  $7.5 \mu s$  later, which should be picked at around the arrow position shown in Figure 3.8, compared to the picked arrival time in the signal at receiver 1.

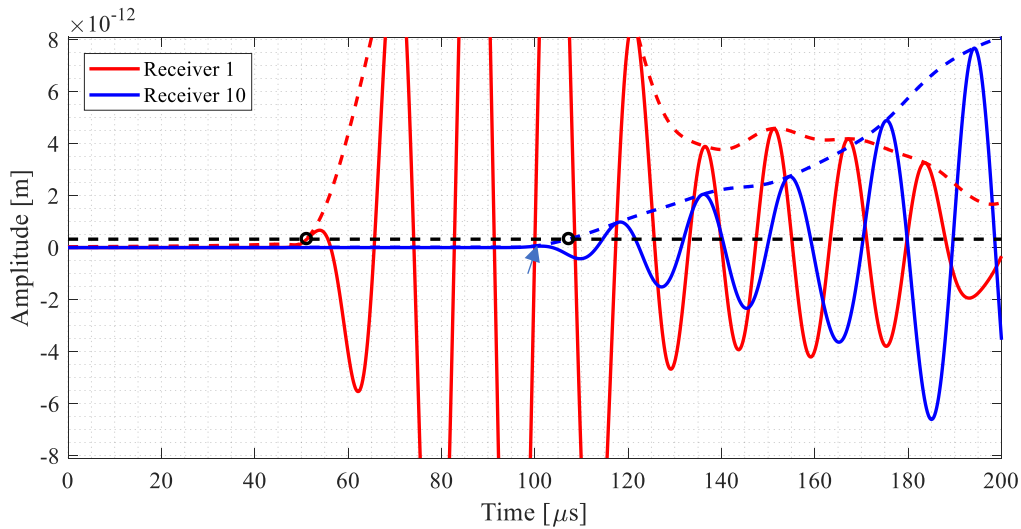


Figure 3.8: Comparison of arrival time picks in signals at receivers 1 and 10

The arrival times of received signals and source signal were calibrated manually according to the onset of arrival time in signal 1. The constant-threshold-picked arrival times and the calibrated results are shown in Figure 3.9 as the blue dots and red dots, respectively. The blue and red dashed lines show the estimated wave speeds according to the constant-threshold-picked arrival times and calibrated results. They were around 4000 m/s and 4400 m/s, respectively. It can be concluded that in a case that the first mode can be detected, the parameter: arrival time can give useful information about travel distance, with an error around 10% by using constant threshold method. This concluding remark is further evaluated in a practical case in section 4.2.

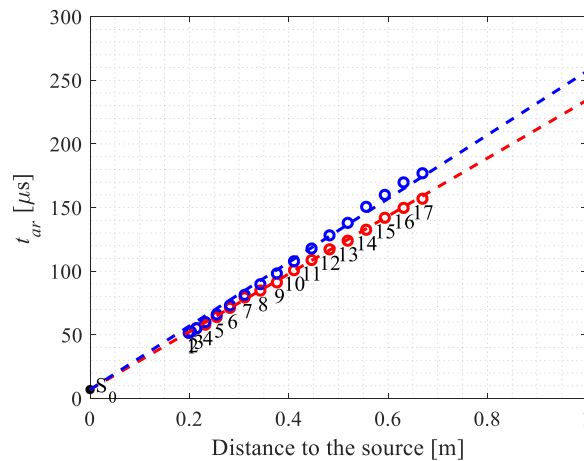


Figure 3.9: Constant-threshold-picked arrival times and the calibrated arrival times

### 3.2.1.2 Peak amplitude

The picking of peak amplitudes can be found to be influenced by the shape of the waveform. Figure 3.10 shows the waveforms at different receivers with different travel distances. The receiver number is shown on the top, corresponding to the travel distance shown in  $x$ -axis. The manually-calibrated arrival times are marked as blue dots, and the times of the peak amplitudes are marked as red dots. It can be seen that the peak amplitudes were not always the maximum amplitude of the first wave mode (e.g. signal 6). It can be caused by reflections (e.g. signals 6,

11, 12, 13, 14), other wave modes (e.g. signals 7, 8, 9, 10), or a combination of multiple wave modes and reflections (e.g. signal 15).

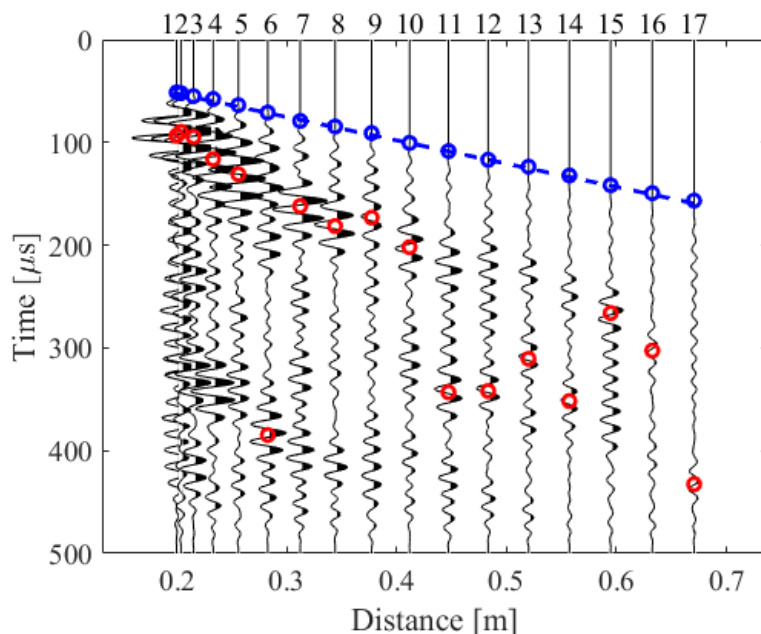


Figure 3.10: Waveforms received at different receivers

The waveform of signal 12 is shown as an example in Figure 3.11, with some parameters marked in the same way as Figure 3.7. As can be seen, the first wave mode (P-wave mode) interfered with the second wave mode (S-wave mode). The peak amplitude was picked later around 340  $\mu\text{s}$  possibly a reflection from the boundary of the beam. The peak amplitude of the first wave mode was less than  $2 \times 10^{-12}$  m, and the picked peak amplitude in parameter-based method was around  $6.5 \times 10^{-12}$  m. Therefore, the peak amplitude in decibel should be corrected

$$\text{at least } dB\left(\frac{2 \times 10^{-12}}{6.5 \times 10^{-12}}\right) = -10.24dB.$$

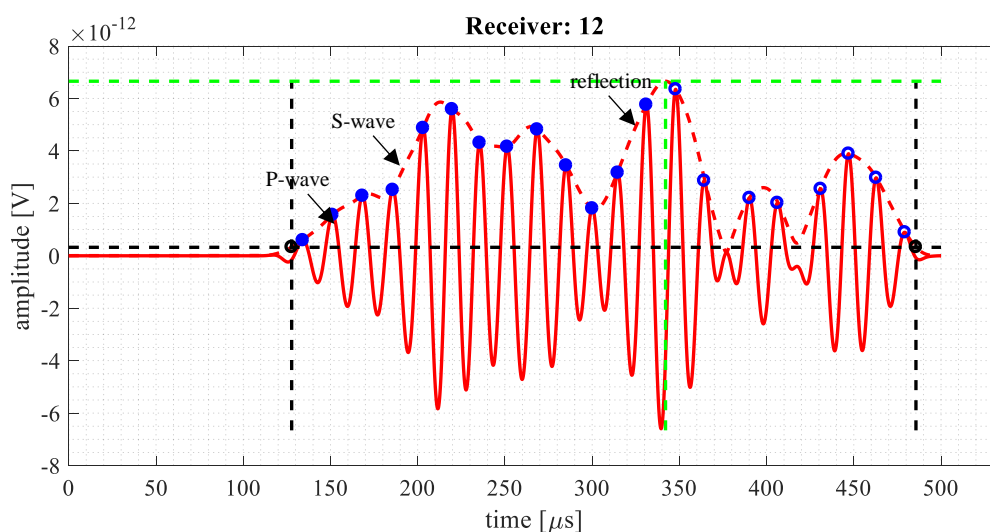


Figure 3.11: Waveform of signal 12 and extraction of parameters

The changing of the peak amplitude can be expressed by the ratio of the peak amplitudes in decibels:

$$ampdrop = dB(A_i) - dB(A_0) = dB\left(\frac{A_i}{A_0}\right) \quad (5.1)$$

where,  $A_i$  is the peak amplitude of signal  $i$ , and  $A_0$  is the peak amplitude of reference signal.

The calculated peak amplitude drops of the received signals from the reference are shown in Figure 3.12. Although a decreasing trend can be observed, it may not be sufficient to draw a reliable conclusion since the peak amplitudes may relate to different wave modes or other reflections.

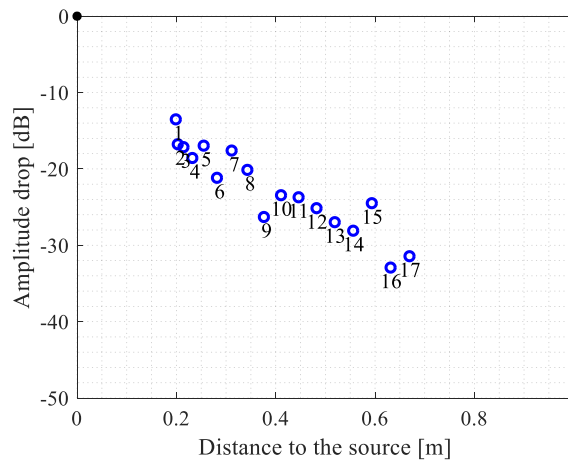


Figure 3.12: Peak amplitude drops

### 3.2.1.3 Rise time, counts to peak, rise energy

These parameters are influenced by the time of peak amplitude according to their definitions. The mispicking of the peak amplitude can make these parameters unreliable. For example, in signal 12 (shown in Figure 3.11), the number of counts to peak was extracted to be 13, while the number of counts to peak for the first wave mode was only 3. The results of counts to peak in the source signal and the received signal are plotted in Figure 3.13. As expected, the data distribution over travel distance was not regular.

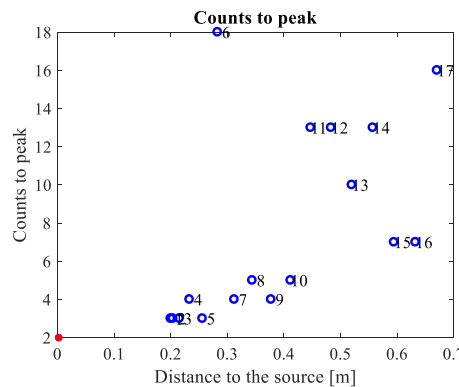


Figure 3.13: Counts to peak

The results of rise time and the drop of rise energy are plotted in Figure 3.14, left and right, respectively. The drop of rise energy in decibels is calculated in dB scale. By comparing the counts to peak, rise time and drop of rise energy, it could be found that a longer rise time will correspond to more counts to peak and less drop of rise energy. It is expected since these values are all related to the pick of the peak amplitude.

It has been studied in some research [14] that the RA value which is the ratio between rise time and peak amplitude can be used for crack classification. It could be further studied experimentally, however, in our simulation, only one type of source was performed. Therefore, the parameter RA value for crack classification is not evaluated in this thesis.

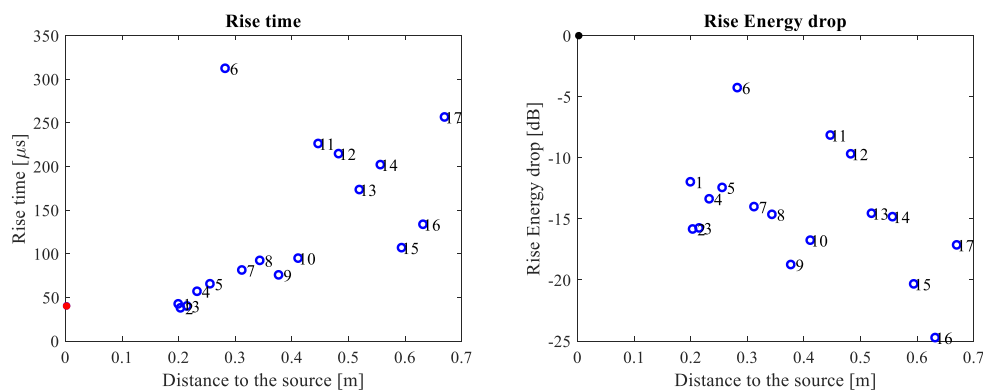


Figure 3.14: Rise time (left) and rise energy drop (right)

### 3.2.1.4 Duration, counts, energy

These parameters are influenced by the threshold level and the waveform. The waveform shape, which can be much influenced by reflections and multiple wave modes, can make the interpretation of these parameters complicated. In a case that the threshold level was so low that nearly the whole waveform was considered, these parameters would be determined by the sample lengths. For example, the duration of signals at receivers 13 and 16 (shown in Figure 3.15) ended both near 500  $\mu\text{s}$ , which was the end of the sample length.

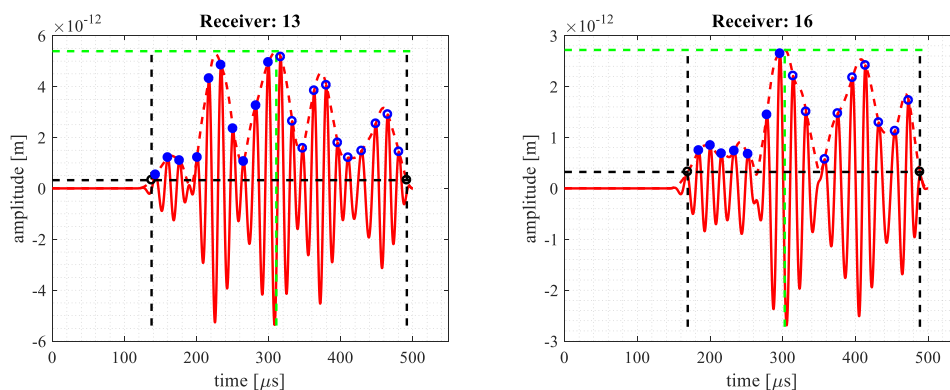


Figure 3.15: Signals in receiver 13 (left) and receiver 16 (right)

## 3.3 Concluding remarks

Wave propagation in a 2D concrete section was simulated and parameters were extracted from the simulated signals following the definitions which are normally-used in parameter-based

method. The performance of parameters over the travel distance was studied. Several conclusions could be acquired and listed below:

- 1) The results indicated that the arrival time could give useful information for the study of wave propagation. A constant threshold method could generate an error of around 10% of the wave speed.
- 2) Waveforms were observed to get complicated by the influence of different wave modes and reflections from boundaries. Therefore, parameters related to arrival of the peak amplitude (e.g. counts to peak) and duration time (e.g. counts) could not be used for the study of wave propagation in most cases since they were sensitive to the shape of the waveform.

Based on these conclusions, in the data processing in the following tests, a signal-based method is used to eliminate the error caused by parameter-based method.



## 4 Experiments

Measurements of the coupling effect, the material attenuation coefficient, and transmission function on several cracks with different widths, as mentioned in Chapter 2, were carried out. The applied transducers were of series R6I-AST by MISTRAS, narrowband and with center frequency of 60 kHz. Therefore, the measured results were on AE signals with a frequency of around 60 kHz. Experiments were conducted on a cracked concrete beam, with length of 10 m, width of 0.3 m, and height of 0.8 m. The concrete class was C65 with compressive strength  $f_{cm} = 68$  MPa and the maximum aggregate size  $d_a = 16$  mm. The beam was pre-cracked in a shear test (not shown). The beam number is R803B1 which can be found in the measurement report [27]. Cracks were marked as partly shown in Figure 4.1. It has to be remarked that measurements were all carried out when the member was unloaded. That means the cracks were partially-closed during the measurements.

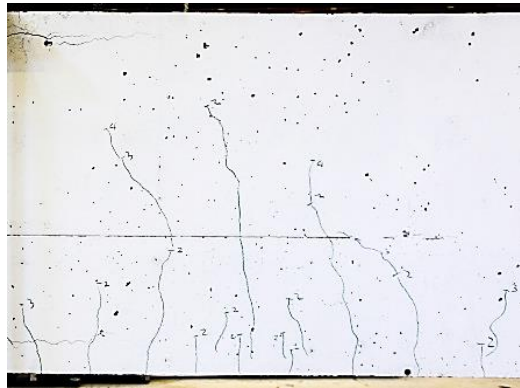


*Figure 4.1: A part of side view of the test concrete beam with several cracks*

### 4.1 Sensor coupling effect

Coupling effect can influence the received AE signals. In AE monitoring, the stability of coupling effect is important for the reliability of the monitoring results. Therefore, a study of the variance of coupling effect, which also includes the unavoidable installation errors, is necessary before applying them in the real conditions.

The couplant used in the measurements in this thesis was a putty-like pressure-sensitive adhesive, shown in Figure 4.2 (1). It is commonly used to attach lightweight objects to hard dry surfaces, and is described as a synthetic rubber compound without hazardous properties under normal conditions. This kind of material is easy to be shaped, which hardly allows voids in the connection. Another consideration is that this couplant is convenient to be removed. The steps of installation and removal are shown in Figure 4.2. The steel bar in step (2) was used to apply the couplant uniformly. The thickness of the couplant can be controlled when applying a same volume of couplant uniformly in a specified area, which can improve the consistency of coupling.

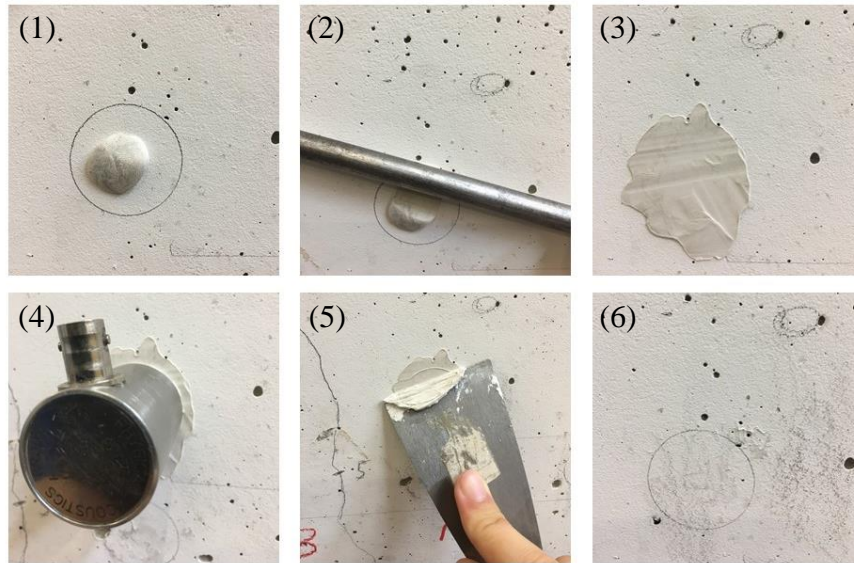


Figure 4.2: Steps of installation and remove (1)-(6) of adhesive putty

To investigate the variance of coupling effect, other influences in Equation (2.8) were designed to be the same. Four sensors were mounted in the un-cracked area to avoid the influence of crack. They were at the four points of a square whose side length was 150 mm. Pencil break (PB) tests were done in the central point of the square. It means that every source-receiver combination had a same travel distance of 106.07 mm. The mold for the sensors positioning and PB test location was pre-fabricated, which improved the accuracy of the tests, see Figure 4.3. Number 1 to 4 indicates the positions of four sensors, and the center of the middle circle is the location of the PB test. Therefore, for a same source, propagation distance and medium, the comparison of the received signals can lead to a result of the variation of coupling effect.

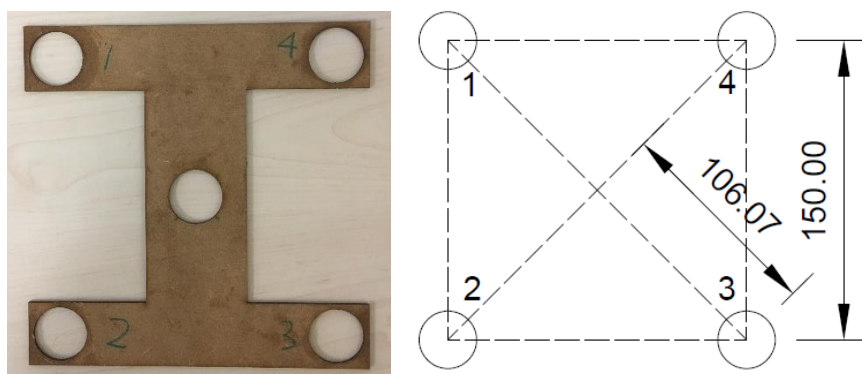


Figure 4.3: Mold of sensors positioning and PB test location (left) and schematic graph (right)

PB tests were performed three times to limit the accidental error. For example, the peak amplitudes in decibel received by sensor 1 in three PB tests were 80 dB, 79 dB and 82 dB, respectively. The average value 80.3 dB was therefore selected to be the peak amplitude received by sensor 1.

The variation of the coupling effect of the four sensors can be described by the coefficient of variation  $c_r$ , which is the ratio of standard deviation  $\sigma$  and mean value  $\mu$  of the peak amplitudes received by the four sensors. Based on the short installation time which is important

for performing a large number of fundamental measurements, six groups of repeatability tests were carried out. In each group, the mean value  $\mu$ , the standard deviation  $\sigma$  and the coefficient of variation  $c_v$  of the peak amplitudes received by the four sensors are shown in Table 4.1.

Table 4.1: Mean value ( $\mu$ ), standard deviation ( $\sigma$ ) and coefficient of variation ( $c_v$ ) of the peak amplitudes received by four sensors

Group	1	2	3	4	5	6
$\mu$ [dB]	84.56	80.22	78.67	79	84.56	82
$\sigma$ [dB]	4.43	3.41	2.68	4.64	2.45	3.07
$c_v$ [-]	0.05	0.04	0.03	0.06	0.03	0.04

An average value of the coefficient of variation was around 0.042. It means that for a mean value of around 85 dB, the amplitude variation caused by couplant was around 4 dB. In the following measurements, an observation of a scattering of 5 dB in the amplitude is therefore considered to be normal.

## 4.2 Transfer function in concrete medium

As shown in Equation (2.8), transfer function  $W$  in concrete medium can influence the received signals. The transfer function relates to the material property and frequency. In this test, the transfer function of the medium in a frequency around 60 kHz was measured on uncracked concrete which was assumed to be homogeneous.

An 1-by-14 array of transducers was arranged with a spacing of 40 mm. The first transducer (from left to right, in Figure 4.4) emitted ultrasonic waves, and the other 13 sensors acquired the responses. Therefore, by comparing the signals received at different locations, the transfer function can be estimated.

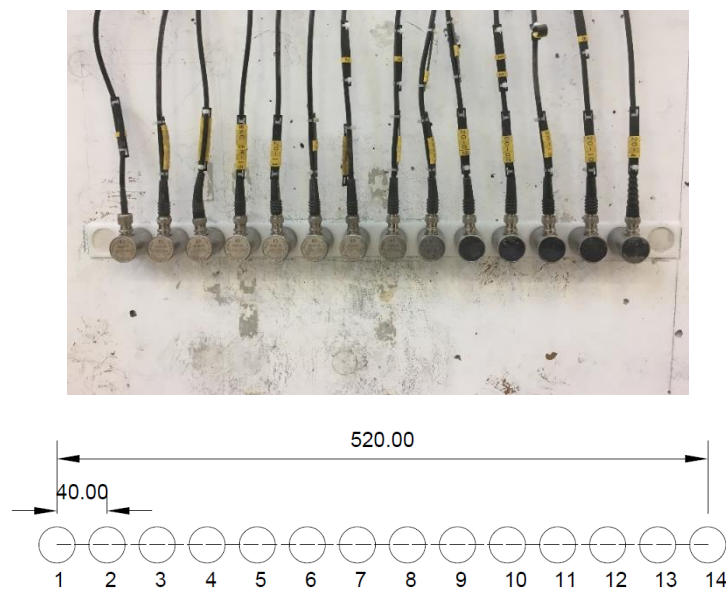


Figure 4.4: Array arrangement: (top) in practice and (bottom) in schematic graph

In the processing of the signals, no additional frequency filter was used. The frequency range was therefore the same as the sensor operating frequency range, which was effectively in a narrow range of [40 100] kHz. Signals were normalized as  $a_i^* = \frac{a_i}{A_i}$ ,  $i \in [1, 2, 3, \dots, 14]$ , where  $a_i$  is the amplitude of signal received by sensor  $i$ , and  $A_i$  is the peak amplitude of signal received by sensor  $i$ . The normalized signals received by sensors 1 to 14 are shown in Figure 4.5. It could be observed that the arrival of the first wave mode attenuated nearly to the noise level when the wave propagated over around 0.5 m at sensors 13 and 14. The signal recorded by sensors 1 was not comparable to others in the beginning part. This was because transducer 1 also emitted waves, which went beyond the dynamic range of the data acquisition system. Therefore, the signal recorded by sensor 2 was set to be the reference.

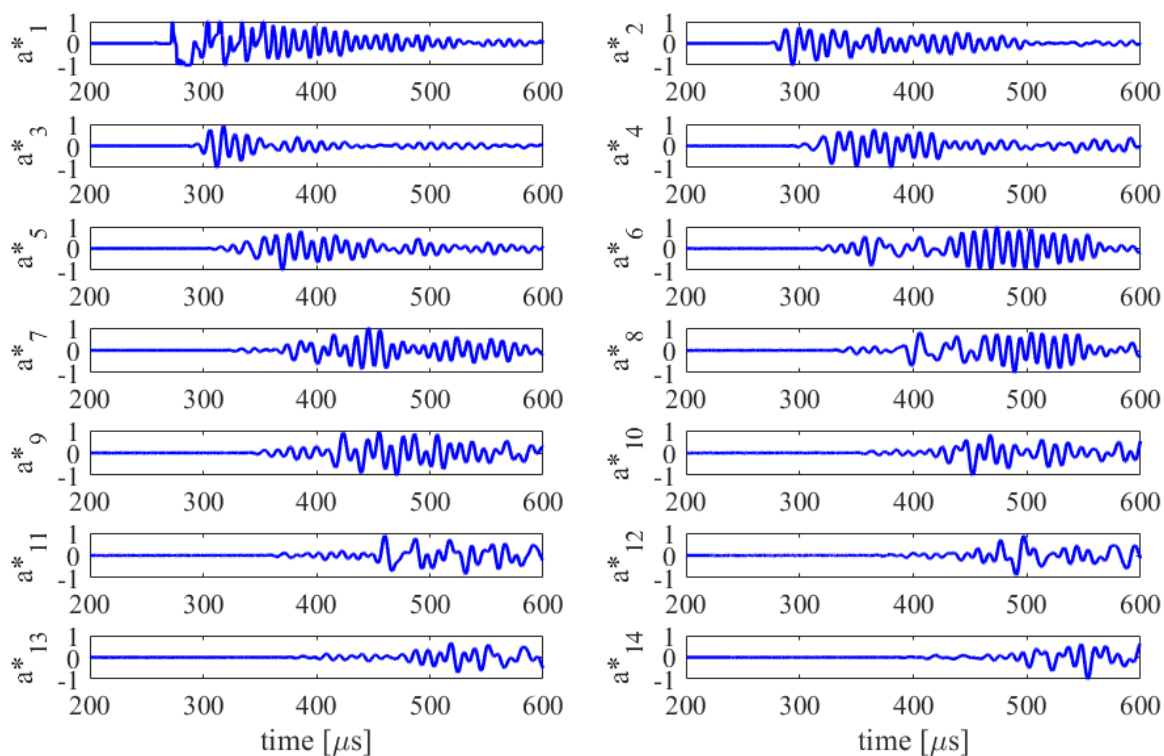


Figure 4.5: Normalized received signals from transducers 1 to 14

Focusing on the first wave mode, the arrival time was picked based on crossing threshold at 5 percent of the peak amplitude of signal received by sensor 2. Travel times from sensor 2 to other sensors were calculated by subtracting the arrival time of the two channels. Figure 4.6 showed the travel time from sensor 2 to sensors 2-14. The wave front traveled at the velocity of P-wave, which was around 4000 m/s and similar to the theoretical calculation in section 2.1. The arrival time was observed to have a scatter of about 5  $\mu\text{s}$ , which was expected considering the time picking accuracy.

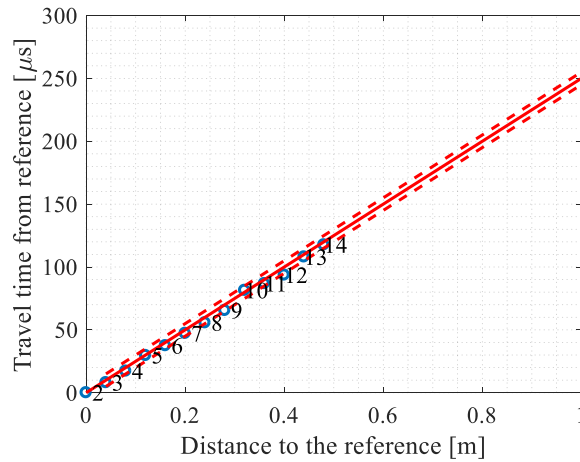


Figure 4.6: Travel time from sensor 2 to sensors 2-14

This test result can also be used to further evaluate the arrival time in parameter-based method in Chapter 3. Since the positive conclusion on the parameter, i.e. arrival time, is based on the simulated results, a further evaluation on the signals from tests including influence of couplant and sensor is necessary.

The arrival times picked by a constant threshold without manually calibration, which is the condition in parameter-based method, are plotted and compared with the calibrated results in Figure 4.7. The blue circles indicate the automatic picking results and the red circles indicate the calibrated results. It can be observed that in sensors 10-14, the automatic arrival times were picked too early, which is expected since that the first wave mode was reduced near the noise level and the picking points may be the noise. For signals whose first wave mode could be successfully detected, the automatic picks by a constant threshold were around 2-5  $\mu\text{s}$  later than the calibrated results. In this test, the wave speed before calibration is around  $0.2\text{m}/55\mu\text{s} = 3636$  m/s, which is around 10% less than the calibrated wave speed. It meets with the conclusion obtained from simulated results that an error of 10% could be generated.

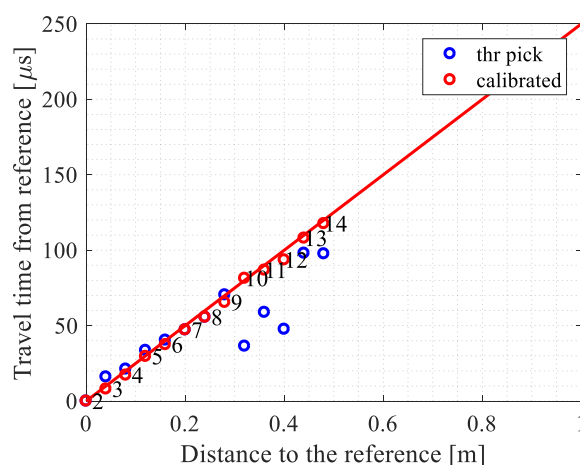


Figure 4.7: Constant-threshold-picked and calibrated arrival times of test in section 4.2

The signals received by sensors 2 to 8 are plotted in Figure 4.8. The red line indicates the envelop of the signals. The surface waves traveled at a lower velocity, shown by the orange

line. It can be estimated that the surface wave velocity was around 2124 m/s which was comparable to the theoretical calculation in section 2.2. The surface waves attenuated slower, thus had a larger contribution to the picked maximum amplitudes. The reflection effect could be neglected, since the distance to the nearest boundary was around 300 mm in this test, which made the reflected waves arrive at least  $0.3 \times 2 / 4000 \times 10^6 = 150 \mu\text{s}$  later. The amplitude drops from the reference are shown in Figure 4.9. The amplitude drop in decibel was calculated as:

$\left| 20 \log \left( \frac{A_i}{A_2} \right) \right|$ , where  $i \in [2, 3, \dots, 14]$ ,  $A_i$  is the peak amplitude in mV of the signal received by sensor  $i$ .

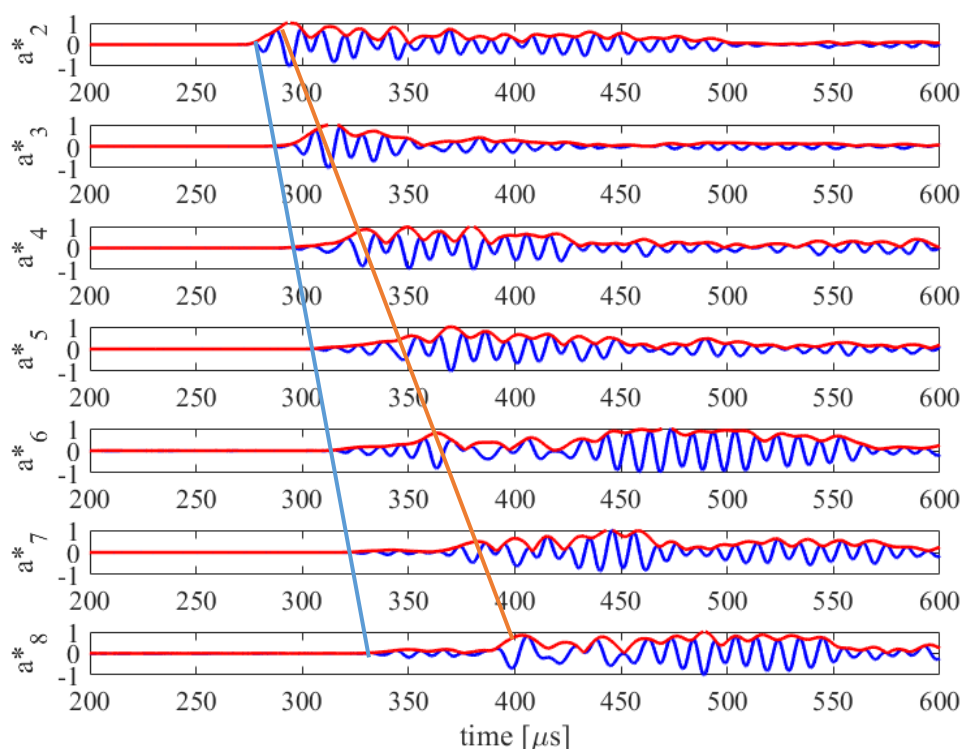


Figure 4.8: P-wave and surface wave arrival time in channels 2-8

The attenuation of surface wave followed the cylindrical spreading rule. By subtracting the theoretical spreading loss from the total attenuation, the material attenuation factor was estimated to be around 20 dB/m at the frequency of around 60 kHz. Therefore, red solid line indicates the sum of theoretical spreading loss and material attenuation. The red dashed curves indicate that the amplitude drops had a scatter of around 5 dB. This was expected since the couplant can cause an amplitude variation of 5 dB.

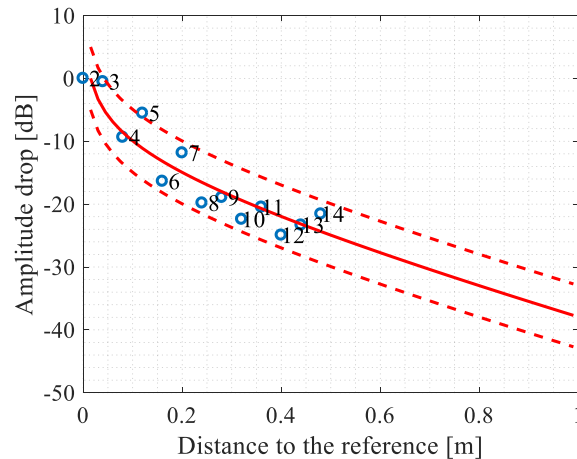


Figure 4.9: Amplitude drops of signals recorded by transducers 2-14

The attenuation of P-wave follows the spherical spreading rule. By combining the spread loss and material attenuation which was around 20 dB/m, the attenuation of body wave within 1 m may be estimated as shown in Figure 4.10 as the black line. It shows that the attenuation of the surface wave and the body wave over 1 m were around 35 dB and 55 dB, respectively, assuming a material attenuation factor of around 20 dB/m at 60 kHz. The evaluation for P-wave attenuation is expected to be conservative since P-waves with larger wavelength are scattered less substantially by the aggregates.

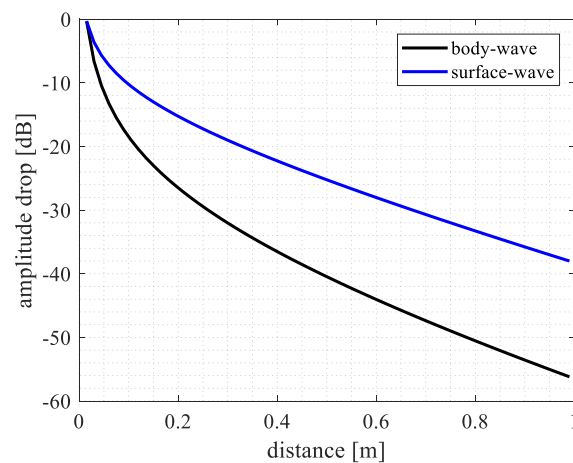


Figure 4.10: Attenuation of body wave and surface wave within 1 m

### 4.3 Transmission function of cracks with different crack widths

The faces of partially-closed cracks may be acoustically coupled and allow some waves travel through. As shown in Equation (2.8), the coupling of a partially-closed crack may be imperfect and have an influence on the received signals. Measurements were designed to control other factors which may influence the received signals except for the travel path, i.e. travel through no crack or travel through a partially-closed crack. By comparing the received signals, whose only difference is the travel path, we can get the transmission function of a partially-closed crack.

Measurements were conducted on eight cracks with different crack widths (i.e. 0.05 mm, 0.1 mm, 0.2 mm, 0.3 mm, 0.6 mm, 1 mm, 1,5 mm and 3 mm). The crack widths were measured on the beam surface by a crack width ruler. Therefore, these values were the surface openings of the cracks. The sensor arrangement for these tests is shown in Figure 4.11: the middle transducer (number 2) emitted ultrasonic waves, and two sensors on the left and right (numbers 1 and 3 at a center to center distance of 80 mm to the middle transducer) acquired the responses. Sensor 1 was placed on the other side of a crack, therefore the signal received by sensor 1 travelled through the crack, compared to the signal received by sensor 3, which was set to be the reference.

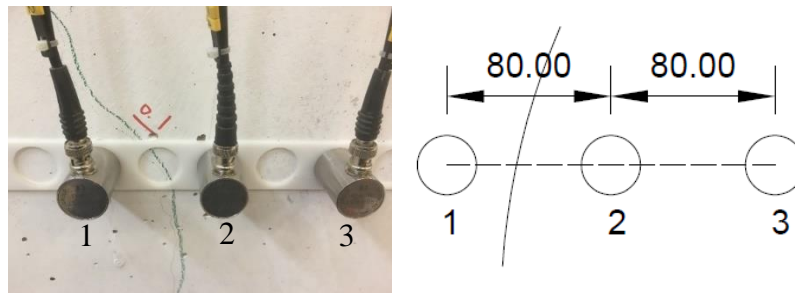


Figure 4.11: Sensor arrangement: (left) in practice and (right) in schematic graph

For each crack, the responses from sensors 1 and 3 were normalized by dividing the peak amplitude of the signal received by sensor 3, shown in Figure 4.12. No additional frequency filter was used. The frequency range was therefore effectively around 60 kHz. To estimate the crack transmission function, the signals with and without (marked as baseline) the influence of crack were compared. The blue baseline shows the reference signal received by sensor 3, which was not influenced by the crack, and the red line shows the signal received by sensor 1 with the influence of crack. A general observation is that the cracks can cause a delay of arrival time and attenuation of the amplitude.

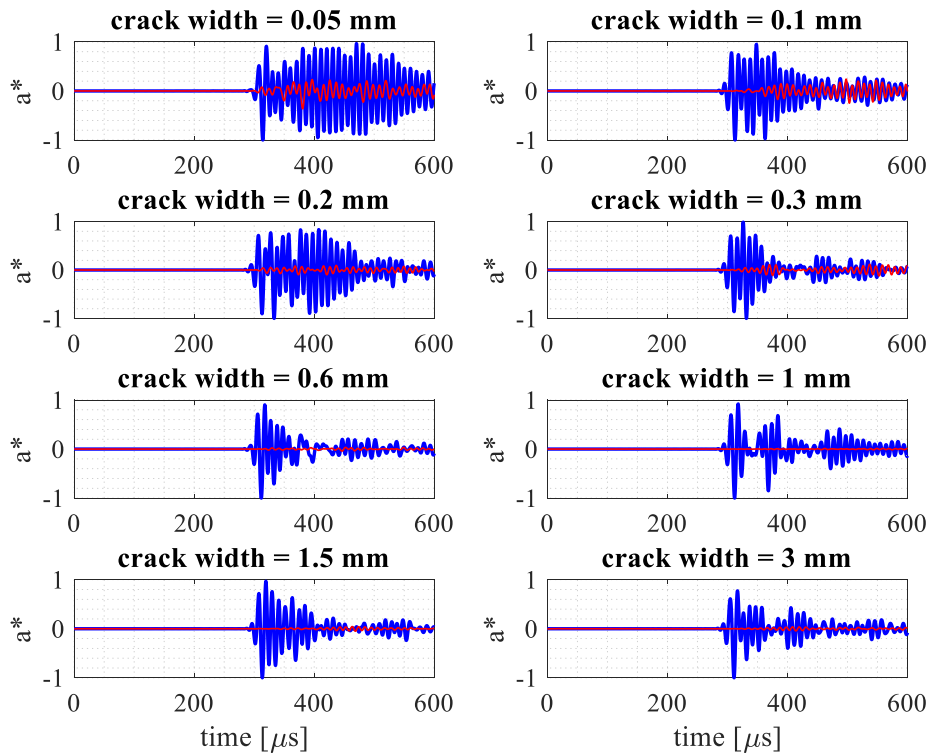


Figure 4.12: Normalized signals received by transducer 3 (baseline) and transducer 1 (cracked line)

For a detailed check, a part of the normalized signals from test of 0.3 mm crack between 260  $\mu\text{s}$  and 330  $\mu\text{s}$  is shown in Figure 4.13 in a zoomed view. Around 20  $\mu\text{s}$  delay of arrival time can be observed.

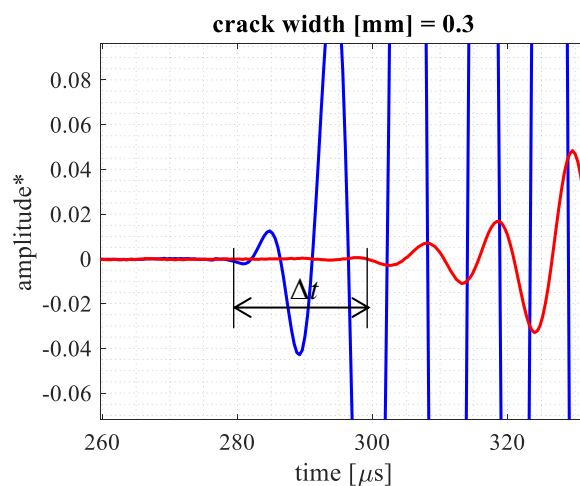


Figure 4.13: Zoomed signals from test of 0.3 mm crack

The arrival time was picked using the same method mentioned in section 4.2. The results showed that the arrival time delay caused by cracks with various surface widths were around 20  $\mu\text{s}$  with a scatter of about 5  $\mu\text{s}$ , shown in Figure 4.14. The drop of the peak amplitude was

calculated as  $\left| 20 \log\left(\frac{A_1}{A_3}\right) \right|$ , where  $A_1$  and  $A_3$  are the peak amplitudes in mV of the signals with and without the influence of the crack, respectively. The amplitude drops caused by cracks

with different surface widths are shown in Figure 4.15. It can be generally observed that the amplitude drop increased with the crack width, approximately ranging from 14 dB to 46 dB.

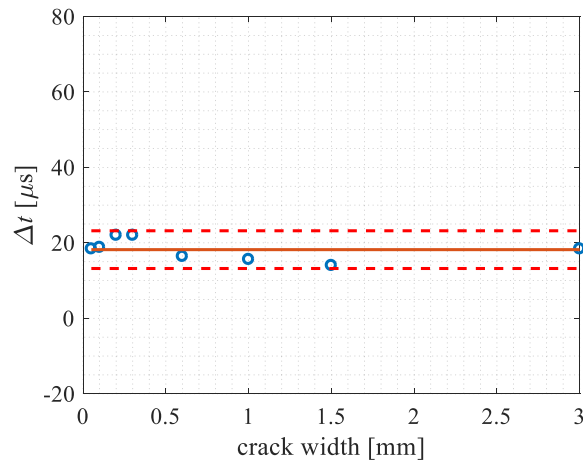


Figure 4.14: Arrival time delays caused by several cracks with different widths

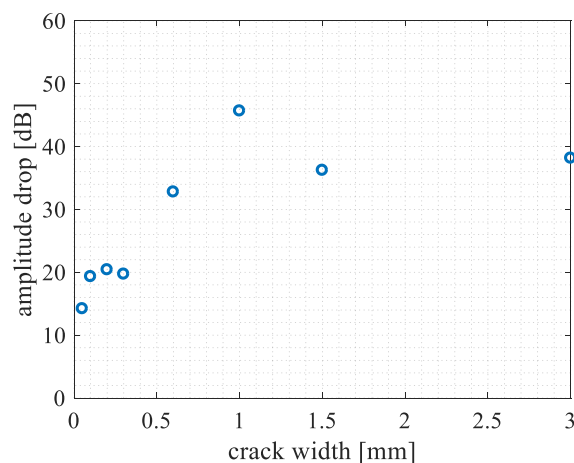


Figure 4.15: Amplitude drops caused by several cracks with different widths

The attenuation within 1 m from the source can be a combination of spread loss, material attenuation and crack influence. From the previous measurements in section 4.2, the material attenuation factor was around 20 dB/m at 60 kHz. Assuming a 0.05 mm wide crack is at a distance of 0.5 m, the amplitude drop in decibels of body wave and surface wave can be compared and shown in Figure 4.16. It indicates that when a narrow partially-closed crack of width 0.05 mm is present, the attenuations of the surface wave and the body wave over 1 m are around 52 dB and 70 dB, respectively. Therefore, for a source with a peak amplitude of 100 dB, the peak amplitude of the signal received at 1 m further becomes 48 dB and 30 dB, respectively. In field measurements, both could be lower than the threshold of the AE system.

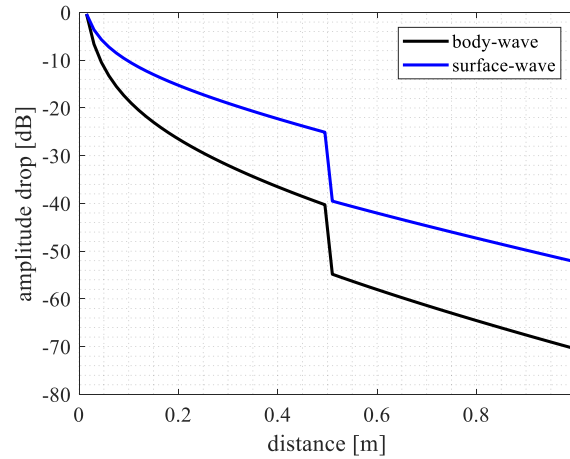


Figure 4.16: Amplitude drop in wave propagation, with a 0.05 mm wide crack at 0.5 m away from the source

#### 4.4 Anisotropic transmission function of several cracks

Micro cracks in the cracked concrete could induce anisotropic mechanical properties [28]. Therefore, the transmission function of a crack could also be anisotropic. Measurements were designed to test the anisotropic influence of crack on the AE signals.

In this measurement, sensors were arranged to receive the signals which propagate through a same crack but in different directions, shown in Figure 4.17. Transducer 2 emitted ultrasonic waves, and sensors 1, 3, 4, 5 received signals in directions of  $-180^\circ$ ,  $0^\circ$ ,  $45^\circ$ ,  $90^\circ$  to  $\mathbf{n}_0$  (the normal direction of the crack plane, shown with the black arrow in Figure 4.17), respectively. Five cracks with different crack widths (i.e. 0.05 mm, 0.1 mm, 0.2 mm, 1 mm, 2 mm) were tested.



Figure 4.17: Sensor arrangement with the transducer in the middle and the receivers around

Responses in four directions, which were at  $-180^\circ$ ,  $0^\circ$ ,  $45^\circ$ ,  $90^\circ$ , were recorded. Signal received by sensor 1 was set to be the reference in each test (which was not directly influenced by the crack). Responses were normalized by dividing the peak amplitude of the signal received by sensor 1 in each test. The normalized signals are shown in Figure 4.18. The blue line is the baseline, showing the signal received by sensor 1. The red lines are the signals received from other sensors. Each row shows the responses in one test. The first column compares the signal received by sensor 3 (in direction of  $0^\circ$ ) to the reference, the second column compares the signal received by sensor 4 (in direction of  $45^\circ$ ) to the reference, and the third column compares the signal received by sensor 5 (in direction of  $90^\circ$ ) to the reference. It can be observed that

when the signal propagated parallel to the crack, the signal amplitude and arrival time were less influenced. The signal attenuated strongly when it propagated through the crack in directions of  $0^\circ$  and  $45^\circ$ .

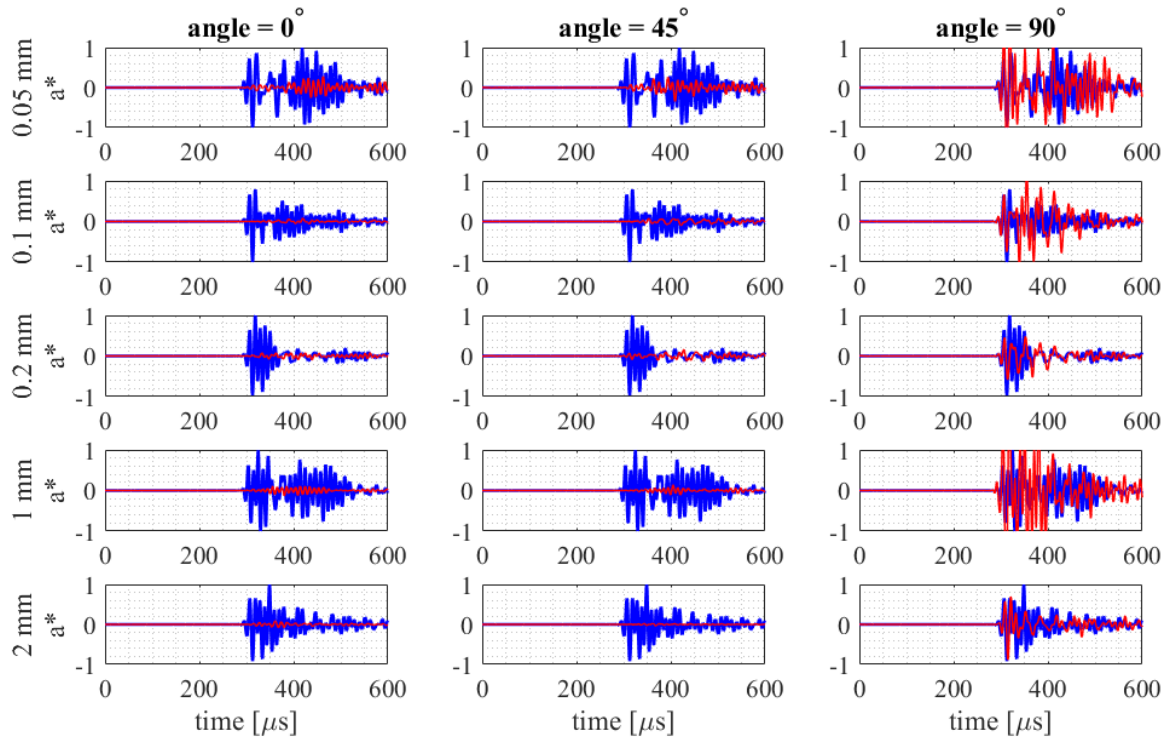


Figure 4.18: The normalized signals received by sensor 1 (baseline), sensors 3, 4, 5 (cracked line) in different directions

The arrival times were picked using the same method mentioned in section 4.2. Arrival time delay and amplitude drop compared to the reference were calculated as  $\Delta t = t_i - t_1$  and

$\left| 20 \log\left(\frac{A_i}{A_1}\right) \right|$ , respectively, where  $t_i$  and  $A_i$  were the arrival time and peak amplitude of signal received by sensor  $i$ , respectively. They were categorized by angles between wave travel direction and  $\mathbf{n}_0$  (shown in Figure 4.19 and Figure 4.20).

Arrival time delays in the orthogonal and parallel directions to the crack (respectively shown in red and blue dots) were observed to be around  $20 \mu\text{s}$  and  $5 \mu\text{s}$  respectively, over a traveling distance of 80 mm, as shown in Figure 4.19. This results show that the crack had an anisotropic transmission effect on the AE signal. The wave front traveled at the speed of P-wave, which was around 4000 m/s from the measurements in section 4.2. Assuming a crack band width of 48 mm with anisotropic properties [29], the speeds in the orthogonal and parallel directions to the crack were calculated to be around 1500 m/s and 3200 m/s, respectively. Black dots in Figure 4.19 indicate the arrival time delays in 45 degrees to the crack. It shows a variance between  $5 \mu\text{s}$  and  $25 \mu\text{s}$ .

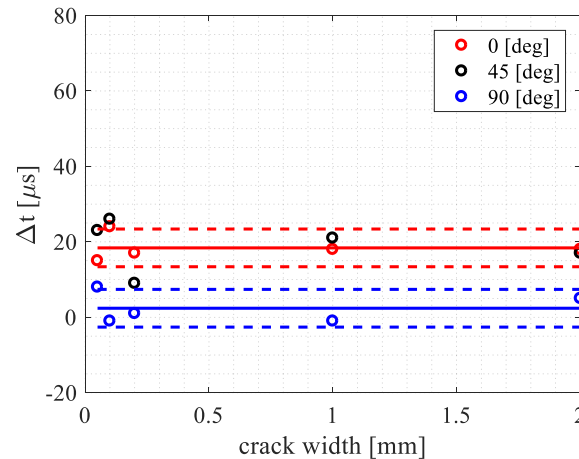


Figure 4.19: Arrival time delays caused by several cracks with different widths and angles, categorized by angle

Amplitude drops in the direction parallel to the crack (shown as blue dots in Figure 4.20) were observed to be negligible. A scatter of about 5 dB can be seen, which could be the couplant variance. In the orthogonal and 45° directions (shown as red and black dots in Figure 4.20, respectively), amplitude drops were approximately ranging from 15 dB to 35 dB, when wave propagated through cracks with widths in the range [0.05 2] mm.

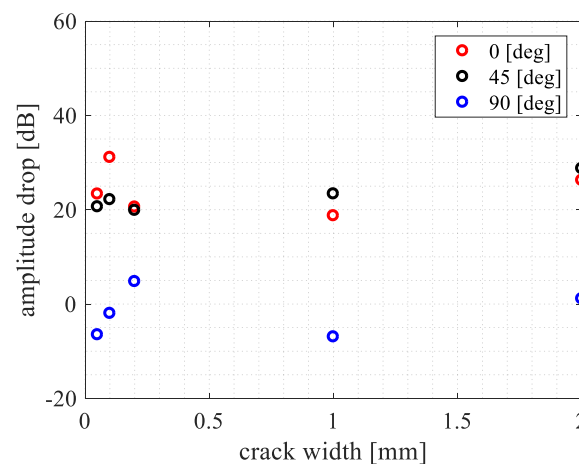


Figure 4.20: Amplitude drops caused by several cracks with different widths and angles, categorized by angle

## 4.5 Concluding remarks

The following conclusions can be made from this chapter:

- 1) A viscoelastic adhesive couplant was used in the measurements. It was found that the variation of the coupling effect was limited to 5 dB for mean amplitude of 85 dB.
- 2) From the 1-by-14 array test on the un-cracked part of the specimen, the speed of the front wave in the concrete medium was around 4000 m/s and the material attenuation factor of the specimen was around 20 dB/m at a frequency around 60 kHz. The attenuation of body waves and surface waves over 1 m were estimated to be around 35 dB and 55 dB, respectively.

- 3) A partially-closed crack with surface openings in the range [0.05 3] mm could cause an arrival time delay of around 20  $\mu$ s and an attenuation from 14 dB to 46 dB. Combining with the attenuation in concrete medium, we can conclude that more cracks may not necessarily lead to more AE activities.
- 4) The influence of cracks on the AE signals was observed to be anisotropic. In the direction parallel to the crack, the wave speed was around 80% of the original speed and the attenuation was negligible, while in the direction perpendicular to the crack, the wave speed was reduced to around 37% of the original speed and the attenuation was in the range [15 35] dB when the crack width was in the range [0.05 2] mm.

## 5 Source Localization

One of the objectives of AE monitoring is to estimate the source location, which is called source localization. An important issue is to evaluate the accuracy and reliability of the localization results. The arrival-time-based localization method, which is introduced in this chapter, is one of the commonly used methods. In this method, factors which could influence the recorded arrival times may influence the localization results. In concrete structures, the cracks can influence the arrival times, thus is one of the main concerns in the evaluation of source localization.

In practice, two status of cracks may occur, one is fully-open crack and the other is partially-closed crack, which have been introduced in Chapter 2. A fully-open crack has acoustically decoupled faces [21] which don't allow waves to pass through. Therefore, tip-diffracted waves are received in this situation. However, a partially-closed crack can allow partial transmission of AE signals, as observed in the former chapter. Therefore, the influences of open crack and closed crack on source localization are studied. Furthermore, the influence of some other uncertainties, for example, the arrival time picking accuracy, are also evaluated.

### 5.1 Localization methods

#### 5.1.1 Analytical solution

In the arrival-time-based localization method, three inputs are needed in most cases. They are the locations of the sensors, the arrival times recorded in sensors, and the wave velocity in the medium. There are other types of localization methods which can work with unknown wave velocity such as optimization based technique [11], but not discussed in this thesis.

A basic assumption is that the concrete medium is homogeneous and isotropic. Therefore, waves travel on straight paths in the medium with a constant speed.

For an AE event at location  $\mathbf{x}_s$ , the elastic waves generated by the source are received by  $N$  transducers attached to the surface of the specimen. The locations of the transducers are denoted as  $\{\mathbf{x}_{R,1}, \mathbf{x}_{R,2}, \dots, \mathbf{x}_{R,N}\}$ . The recorded arrival times are denoted as  $\mathbf{t} = \{t_1, t_2, \dots, t_N\}$ . The speed of the fastest wave mode is assumed to be constant and specified by  $c$ . The relationship among the three inputs is:

$$\|\mathbf{x}_s - \mathbf{x}_{R,i}\| = c \cdot (t_i - t_0), \forall i \in [1, 2, \dots, N] \quad (4.1)$$

where,  $t_0$  is the unknown source time. Combination of the above equations for arbitrary two sensors  $i$  and  $j$  can eliminate the unknown part  $t_0$ :

$$\|\mathbf{x}_s - \mathbf{x}_{R,i}\| - \|\mathbf{x}_s - \mathbf{x}_{R,j}\| = c \cdot (t_i - t_j), \forall i, j \in [1, 2, \dots, N] \quad (4.2)$$

In a two dimensional localization problem, at least three sensors are required. Analytical solutions for Equation (4.2) can form a hyperbolic curve, which is visualized in Figure 5.1. The

red line is the solutions from sensor pairings 1 and 2, the blue line indicates the results from sensor pairings 1 and 3. The green line shows the solutions from sensor pairings 2 and 3. The intersection is the estimated source location.

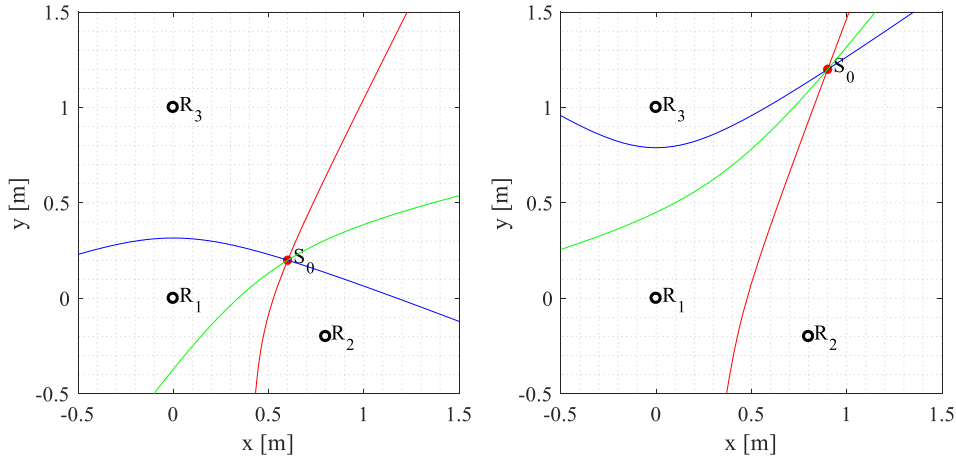


Figure 5.1: Visualization of 2D source localization using Equation (4.2), with three sensors on the surface, AE source inside the detection area (left) and AE source outside the detection area (right)

In a three dimensional localization problem, analytical solutions for the cubic equation (4.2) can form a hyperbolic surface. In an ideal condition, all hyperbolic surfaces determined by different sensor pairings intersect at one point, which is the source location.

### 5.1.2 Grid search method

In the grid search method, the domain is discretized by a particular grid. The distance from a grid point at  $\mathbf{x}_G$  to each sensor can be calculated. The comparison of the calculated differential distances to the measured differential distances can be used to determine the most likely source location. The best fitted grid point can be picked by minimizing the residual between calculated and measured differential distances:

$$r(\mathbf{x}_G) = \sum_{i=1}^{N-1} \sum_{j=i+1}^N \left( \|\mathbf{x}_G - \mathbf{x}_{R,i}\| - \|\mathbf{x}_G - \mathbf{x}_{R,j}\| - c \cdot (t_i - t_j) \right)^2 \quad (4.3)$$

The localization accuracy partly relates to the grid size. In the 2D localization shown in Figure 5.1(left), a grid size of 0.15 m is applied for example, as shown in Figure 5.2, and the best matched grid point is picked as  $S_0^*$ . Therefore, an error of 0.05 m is caused by the 0.15-m-large grid size. Practically, the specimen can be divided more exquisitely. The grid size can be reduced to around 5 mm for example, which will cause less error. Furthermore, the grid size may also be selected depending on the available computer memory and desired solution time. The decision of the grid can be an overall consideration of the accuracy, computation power, and computation time.

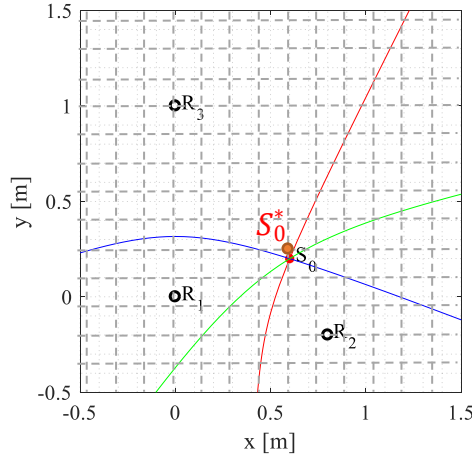


Figure 5.2: The grid search method

### 5.1.3 Localization error

The recorded arrival times highly influence the result of source localization. In existing concrete structures, cracks can additionally influence the arrival times. The recorded arrival times can be described by the summation of the expected arrival time  $\mathbf{t}$  in the undamaged specimen and the additional time  $\Delta \mathbf{t} = \{\Delta t_1, \Delta t_2, \dots, \Delta t_N\}$ :

$$\mathbf{t}^* = \mathbf{t} + \Delta \mathbf{t} \quad (4.4)$$

By plugging the recorded arrival times  $\mathbf{t}^*$  in Equation (4.2) or Equation (4.3), a possibly-erroneous source location is calculated as  $\mathbf{x}_S^*$ . The localization error is hence defined as the distance between the real source location and the calculated source location:

$$error = \|\mathbf{x}_S - \mathbf{x}_S^*\| \quad (4.5)$$

The error in arrival times may also come from other uncertainties. Generally, these uncertainties include the accuracy of time picking, the accuracy of velocity model, the accuracy of sensor coordinates, etc.. The influences of some of these uncertainties are discussed further in this chapter.

## 5.2 Analytical study

The localization method outlined in Section 5.1 was implemented to numerically study the influence of cracks on the accuracy and reliability of AE assessment. A beam with length of 3000 mm, width of 400 mm, and height of 400 mm was modeled. Four sensors were considered on the surface of the beam in six different layouts, as illustrated in Figure 5.3 : two 3D layouts each with a coverage area of 1000 mm×300 mm×400 mm (area enclosed by the sensors), three 2D layouts each with a coverage area of 1000 mm×300 mm, and one 1D layout with a coverage distance of 1000 mm. The 2D layouts and 1D layout are particularly relevant for some practical cases with one-side access only. A crack at  $x=1333$  mm was assumed, shown as the gray surface in Figure 5.3. The crack height was assumed to be 320 mm, which was around 80% of the

beam height, inspired by the ratio of crack height and beam height observed on the test beam in Chapter 4.

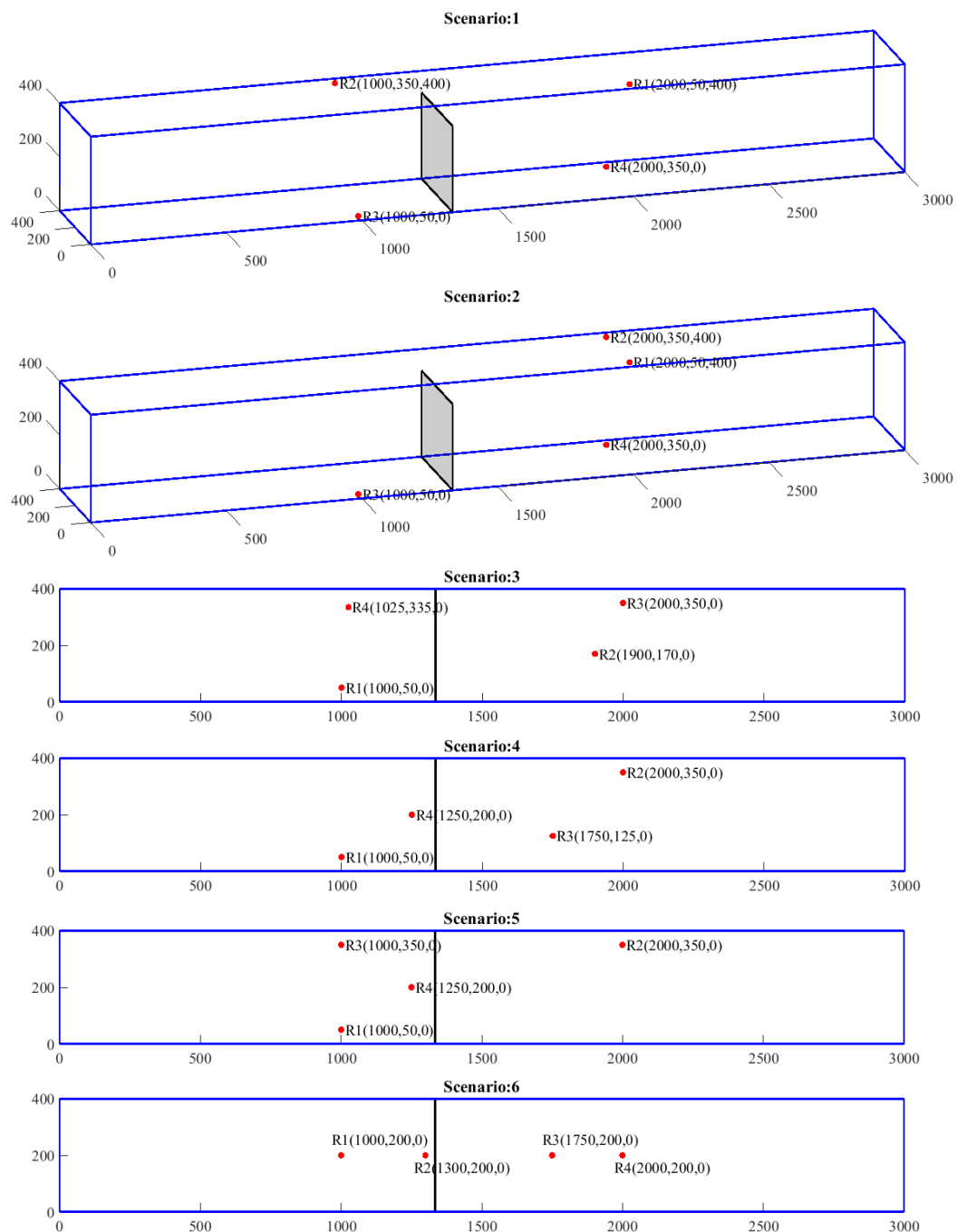


Figure 5.3: Sensor layouts

By applying the grid search method, the detection volume of 1000 mm×300 mm×400 mm was discretized by a uniform mesh of size 5 mm. For each sensor layout, a total number of 165 source locations were uniformly chosen in the detection volume (on a grid of 11×3×5). The source locations are shown by black dots in Figure 5.4. It can be seen that 3D sensor layouts can encompass all sources, 2D sensor layouts can encompass sources on the bottom surface, and 1D sensor layout can enclose sources in that line. For each source, the arrival times (including the crack effect) were calculated first. Next and assuming a baseline situation, the

grid point with the minimum computed residual described by Equation (4.3) was marked as the calculated source. The localization error (Equation (4.5)) was then the distance between the calculated source and the chosen source.

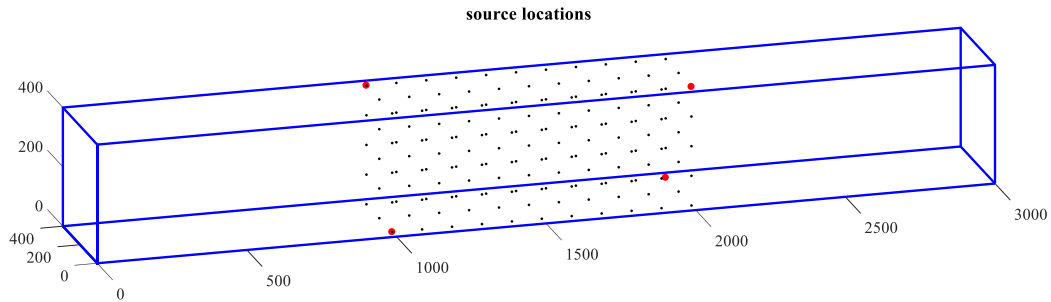


Figure 5.4: The source locations

## 5.3 Results

### 5.3.1 Accuracy of localization for partially-closed cracks

The partial transmission of AE signals by a closed crack relates to the stiffness degradation at the crack. According to the theory of crack band [29, 30], the stiffness is decreased around the crack and a homogeneous and anisotropic band with width of  $w_{cb} = 3 \times d_a$  and an additional tip height of  $l_{ct} = 3 \times d_a$  are assumed, where  $d_a$  is the maximum aggregate size. Considering the maximum aggregate size of  $d_a = 16\text{mm}$ , a crack band with width of  $w_{cb} = 48\text{mm}$  and an additional tip height of  $l_{ct} = 48\text{mm}$  was assumed and illustrated in Figure 5.5. The red line shows the crack and the grey area shows the crack band.

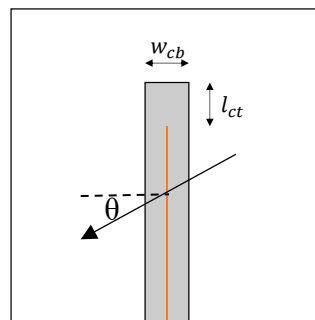
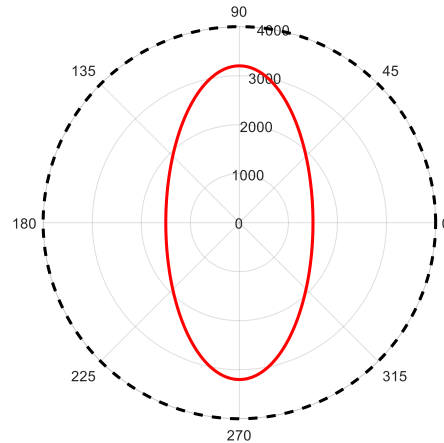


Figure 5.5: Crack band

From the test results in section 4.4, P-wave speeds in orthogonal and parallel directions to the crack were around  $1500\text{ m/s}$  and  $3200\text{ m/s}$ , respectively, which were around 37.5% and 80% to the P-wave speed in concrete medium. The angle-dependent wave speed distribution in the crack band was assumed to conform with the elliptical anisotropy, which can be expressed as:

$$c(\theta) = \frac{c_x c_y}{\sqrt{c_y^2 \cos^2(\theta) + c_x^2 \sin^2(\theta)}} \quad (4.6)$$

where,  $c_x$  and  $c_y$  are the wave speeds in orthogonal and parallel directions to the crack, respectively,  $\theta$  is the angle between wave travel direction and crack surface normal direction, shown in Figure 5.5. The wave speed distribution is illustrated in polar system in Figure 5.6. The black dashed line shows the original wave speed in concrete medium and the red line shows the crack-reduced wave speed. The wave speed declined most in the direction of  $\theta = 0^\circ$  and least in the direction of  $\theta = 90^\circ$ .



*Figure 5.6: Angle-dependent wave speed distribution*

Based on the former assumptions of crack band and wave velocity model, the localization errors for the 165 sources in each layout were calculated. An approximately normal distribution was observed in each layout, as shown in Figure 5.7, with a mean value indicated by a red hollow dot.

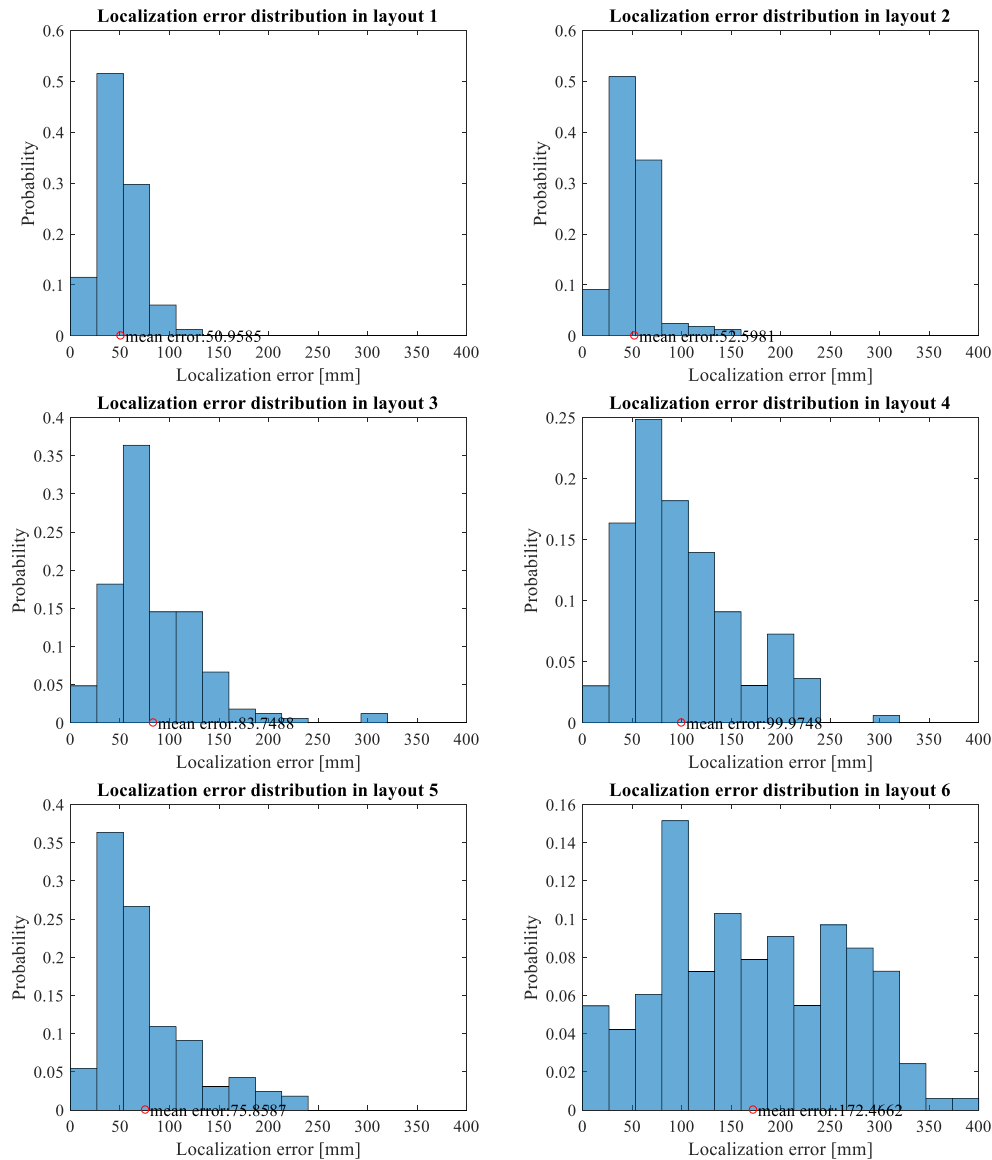


Figure 5.7: Probability distribution of localization errors

The distributions show that for 3D and 2D layouts, source localization errors were mostly around 50 mm. The error deviation in 3D layouts was smaller than that in 2D layouts. The localization errors in 1D layout had a more dispersive distribution, with a mean value around 170 mm and a maximum value around 400 mm.

The maximum localization errors indicated the localization cases with the largest errors. They are summarized in Figure 5.8. For 3D, 2D and 1D sensor layouts, the maximum errors turned out to be about 140 mm, 280 mm and 380 mm, respectively. The worst localization results of layout 2, layout 4 and layout 6 are graphically shown in Figure 5.9. The black star indicates the calculated source location, and the red hollow circle indicates the modeled source location. The gray surface shows the crack and the black frame indicates the crack band zone.

The error in layout 6 is dominated by the  $y$  and  $z$  components. This was expected since the sensors are all located in one line that does not encompass the source. The error in layout 4 was dominated by the  $z$ -component, since the sensors are all located in the bottom surface and the source is outside the area enclosed by sensors. The error in the 3D layouts turned out to be

limited to 150 mm, which occurred when the source was at the boundary of the detection volume.

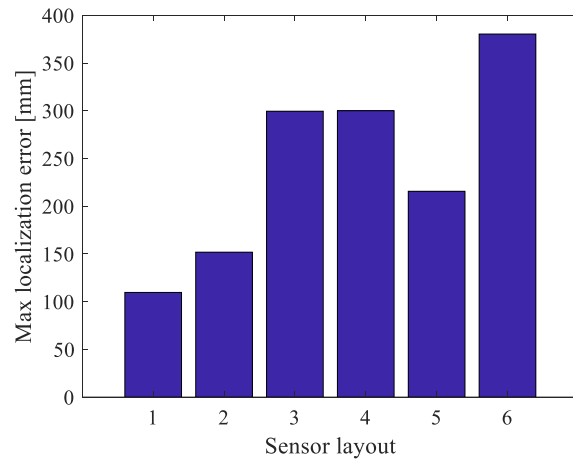


Figure 5.8: Maximum localization error in each layout

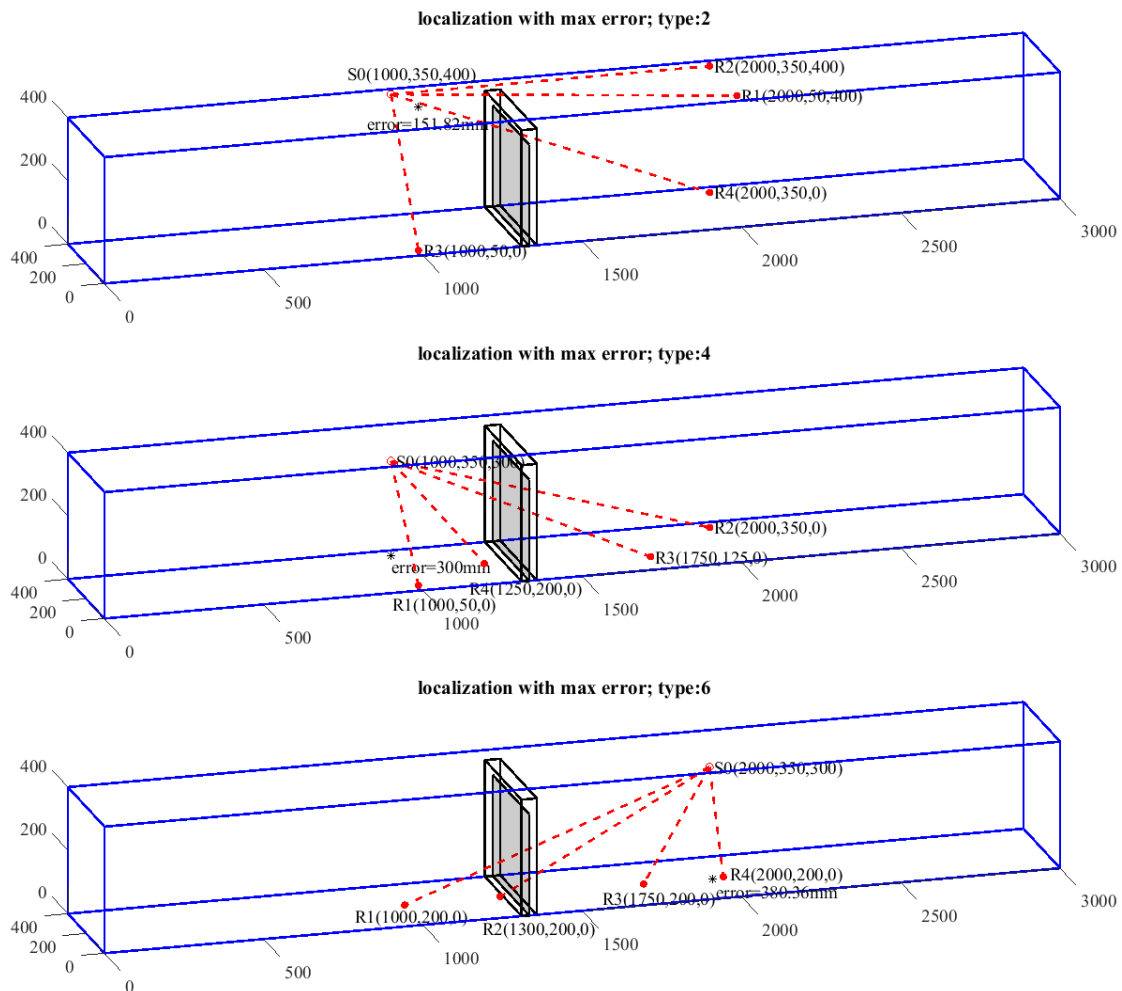


Figure 5.9: Maximum localization error in (top left) layout 2, (top right) layout 4, and (bottom) layout 6

Let us denote the magnitudes of the x, y and z components of an error vector as  $e_x$ ,  $e_y$  and  $e_z$  respectively. A comparison of the errors calculated as: (i)  $\sqrt{e_x^2 + e_y^2 + e_z^2}$  which included all components, (ii)  $\sqrt{(e_x + e_y)^2}$  which excluded the z-component, and (iii)  $e_x$  which excluded the y-component and z-component is shown in Figure 5.10. It can be observed that, the maximum values of errors which excluded the z-component (i.e.  $\sqrt{(e_x + e_y)^2}$ ) in 2D layouts (i.e. layouts 3, 4 and 5) and the maximum values of errors which excluded the y-component and z-component (i.e.  $e_x$ ) in 1D layout (i.e. layout 6) were reduced to around 120 mm and 100 mm, respectively, which are comparable to the maximum values of the total error magnitude (i.e.  $\sqrt{e_x^2 + e_y^2 + e_z^2}$ ) in 3D layouts (i.e. layouts 1 and 2). They were in range of [50 150] mm. The mean localization error is reduced to around 50 mm by the exclusion of the component in which direction source was outside the area enclosed by the sensors.

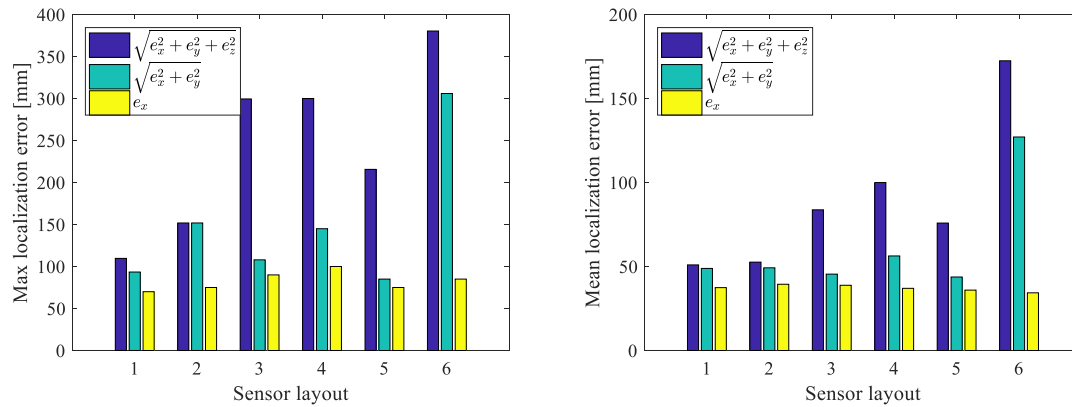


Figure 5.10: Comparison of the maximum errors in different directions (left) and mean errors in different directions (right)

Localization for sources inside the sensor enclosed area is more accurate. In our case, the maximum and mean localization error inside the sensor enclosed area in the corresponding axis was around 100 mm and 50 mm, respectively. In the following discussion in this section, the localization errors were calculated including all components, and the larger errors in 2D layouts and 1D layout were expected.

As observed in Figure 5.9, the maximum localization errors were at the edge of the detection volume, therefore a closer look on the localization errors for inner sources was taken. Eleven uniformly distributed sources in the neutral line of beam were selected and localized. Localization errors for sources on the neutral line in layouts 2, 4 and 6 are plotted in Figure 5.11. The solid blue line indicates the positions of the crack and the dashed blue lines show the sensors positions. Inner source localization had an error of around 50 mm, which was generally more accurate than edge source localization.

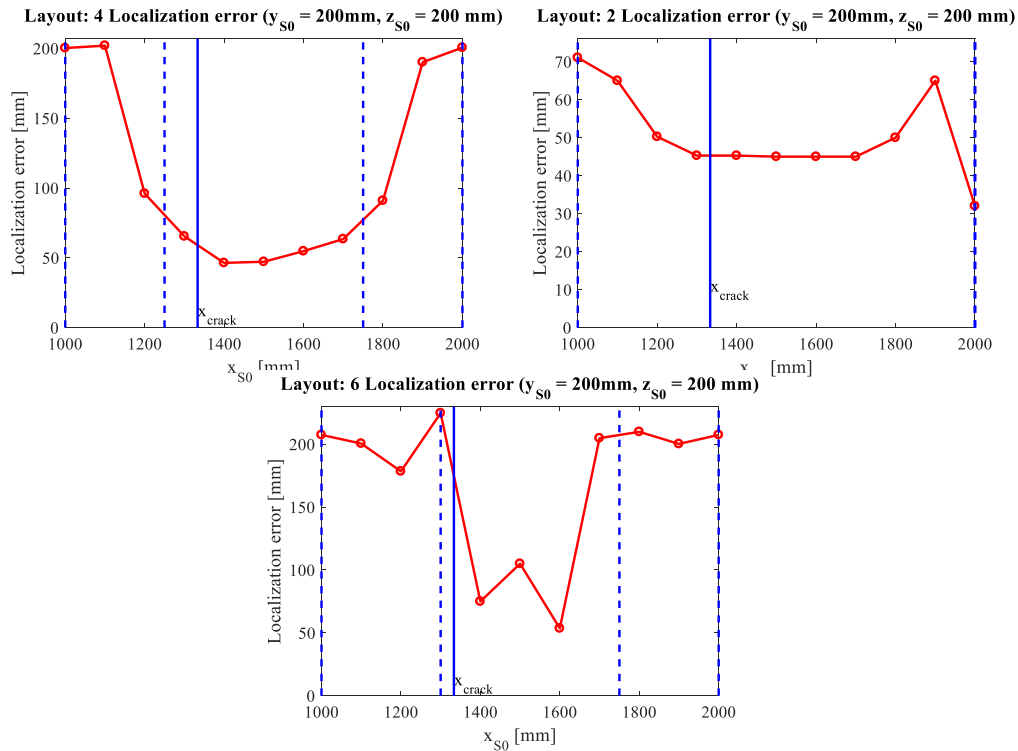


Figure 5.11: Localization errors for sources on the neutral line in layouts 2, 4 and 6

In the above mentioned localization procedure, the accuracy of localization may be further affected by other uncertainties. These uncertainties may be generated from the assumptions of crack band size and wave speed model in crack band. Other general uncertainties (i.e. the accuracy of arrival time picking, the accuracy of sensor locations) may also influence the localization results. The influence of these uncertainties are further discussed.

### 5.3.1.1 Influence of wave speed model in crack band

To study the influence of wave speed distribution in crack band, three cases were analyzed: (i) constant time delay of  $\Delta t = 20\mu s$  in all directions which neglected the angle influence, (ii) elliptical distribution which is described by Equation (4.6), and (iii) linear distribution which is described by Equation (4.7).

$$c(\theta) = c_x + \frac{(c_y - c_x) \cdot \theta}{90}, \theta \in [0, 90] \quad (4.7)$$

where,  $c_x$  is the wave speed in orthogonal direction to the crack,  $c_y$  is the wave speed in parallel direction to the crack,  $\theta$  is the angle between wave travel direction and crack plane normal direction. The two angle-dependent wave speed distribution in range of  $[0, 360]^\circ$  are plotted in Figure 5.12. The red line shows the elliptical distribution, and the blue line shows the linear distribution.

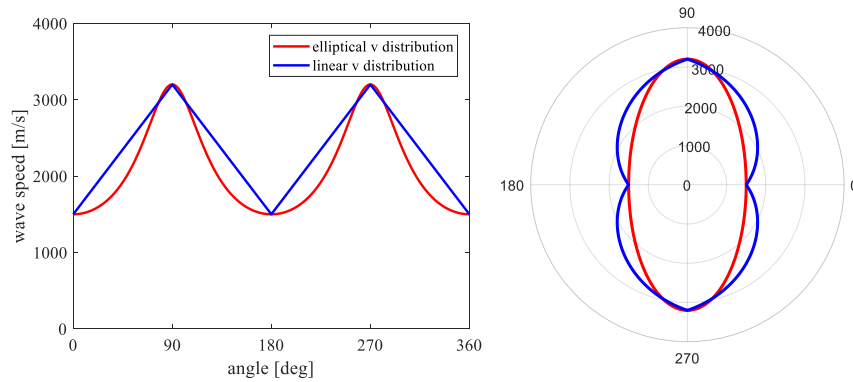


Figure 5.12: Angle-dependent wave speed in crack band in: (left) cartesian system and (right) polar system

The maximum localization errors in three cases were calculated and plotted in Figure 5.13.

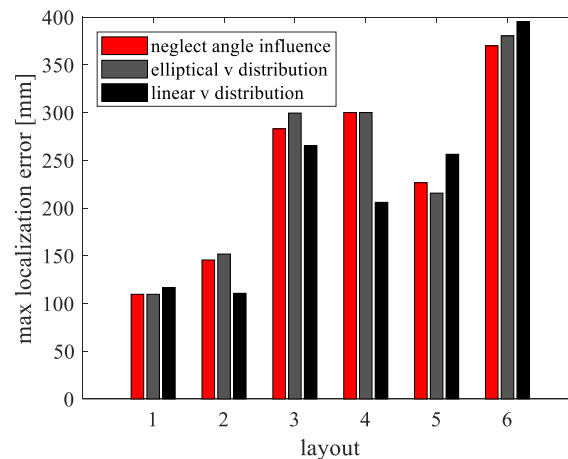


Figure 5.13: Maximum localization error in each layout using different speed models

The maximum localization errors in cases (i) and (ii) were similar and were around 140 mm for 3D layouts, 280 mm for 2D layouts, and 380 mm for 1D layout. The maximum localization errors when assumed a linear wave speed distribution were around 110 mm, 250 mm, and 390 mm for 3D, 2D, and 1D layouts, respectively. It shows that assuming an elliptical distribution was more conservative with around 30 mm more error. The influence of wave speed distribution in crack band on the maximum localization error turned out to be less than 30 mm and could be neglected.

Figure 5.14 shows the localization results of neutral sources in layouts 2, 4 and 6, considering the influence of wave speed distribution. Inner source localization using linearly proportional velocity distribution in crack band had around 20 mm less error in 3D and 2D layouts. In 1D layout, no evident localization difference was observed among the three speed models. The influence of wave speed distribution in crack band on the inner source localization accuracy can be neglected.

As a conclusion, the influence of the wave speed distribution in crack band is negligible and the result generated at the beginning of section 5.3.1 (assuming an elliptical wave speed distribution in crack band) can be more conservative with around 30 mm more error.

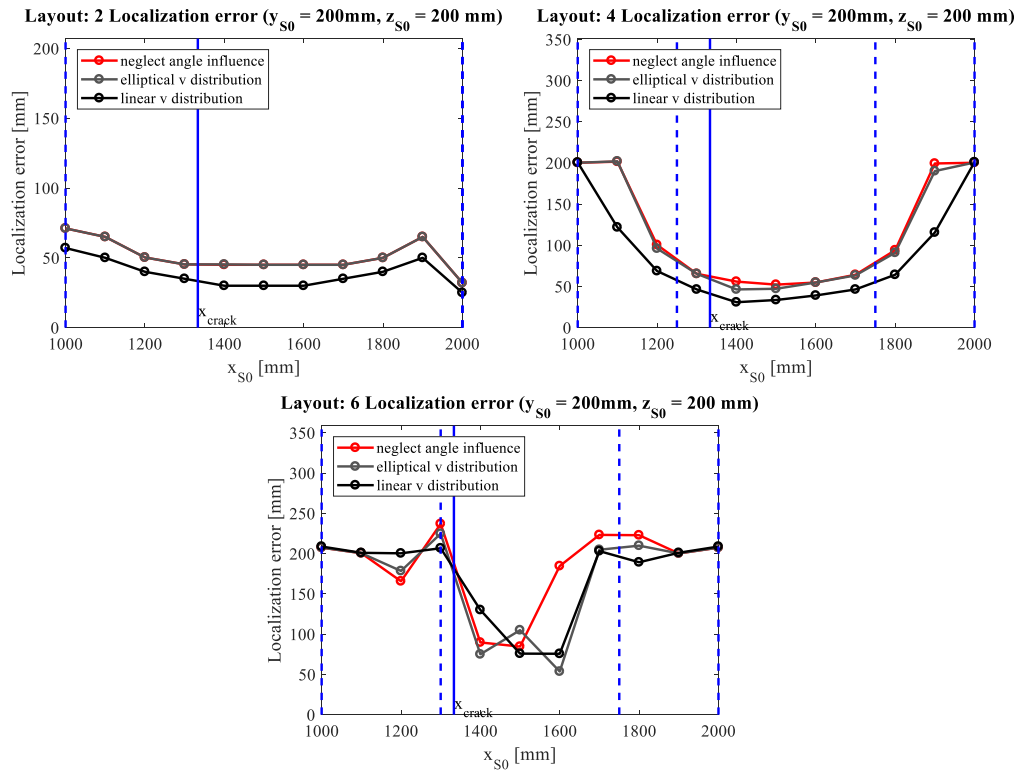


Figure 5.14: Localization errors for sources in the neutral axis using different speed models

### 5.3.1.2 Influence of crack band size

The size of crack band may have a variance around the estimated value in the theory of crack band. A sensitivity study on the effect of crack band size on localization accuracy was performed by changing input values by  $\pm 5\%$ , and  $\pm 50\%$ . The original crack band width was assumed to be  $w_{cb,0} = 3 \times d_a$ , thus the analyzed inputs were  $w_{cb,1} = 0.5 \times w_{cb,0} = 1.5 \times d_a$ ,  $w_{cb,2} = 0.95 \times w_{cb,0} = 2.85 \times d_a$ ,  $w_{cb,3} = 1.05 \times w_{cb,0} = 3.15 \times d_a$ ,  $w_{cb,4} = 1.5 \times w_{cb,0} = 4.5 \times d_a$ . The original crack band length in front of the crack tip was assumed to be  $l_{ct,0} = 3 \times d_a$ , thus the analyzed inputs were  $l_{ct,1} = 0.5 \times l_{ct,0} = 1.5 \times d_a$ ,  $l_{ct,2} = 0.95 \times l_{ct,0} = 2.85 \times d_a$ ,  $l_{ct,3} = 1.05 \times l_{ct,0} = 3.15 \times d_a$ ,  $l_{ct,4} = 1.5 \times l_{ct,0} = 4.5 \times d_a$ .

Maximum localization errors with different crack band widths ( $w_{cb,0}$ ,  $w_{cb,1}$ ,  $w_{cb,2}$ ,  $w_{cb,3}$ ,  $w_{cb,4}$ ) are shown in Figure 5.15. It shows that the maximum localization errors did not change with the crack band widths in layouts 1, 2, 4, 5. In layouts 3 and 6, the influence was less than 40 mm, when the crack band width had a fluctuation of  $\pm 50\%$ .

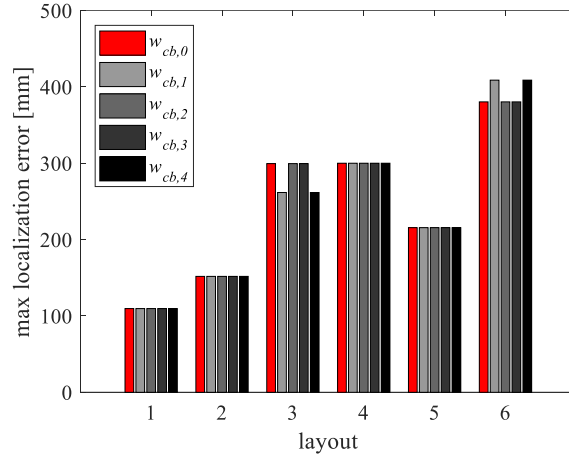


Figure 5.15: Max localization error in each layout with different crack band widths

For inner source localization, the result shows that for 3D and 2D layouts, the localization error hardly had any change when crack band widths changed. For 1D layout, the changing of the output was less than 40 mm, which could be neglected. Examples of layout 2 and layout 6 are shown in Figure 5.16.

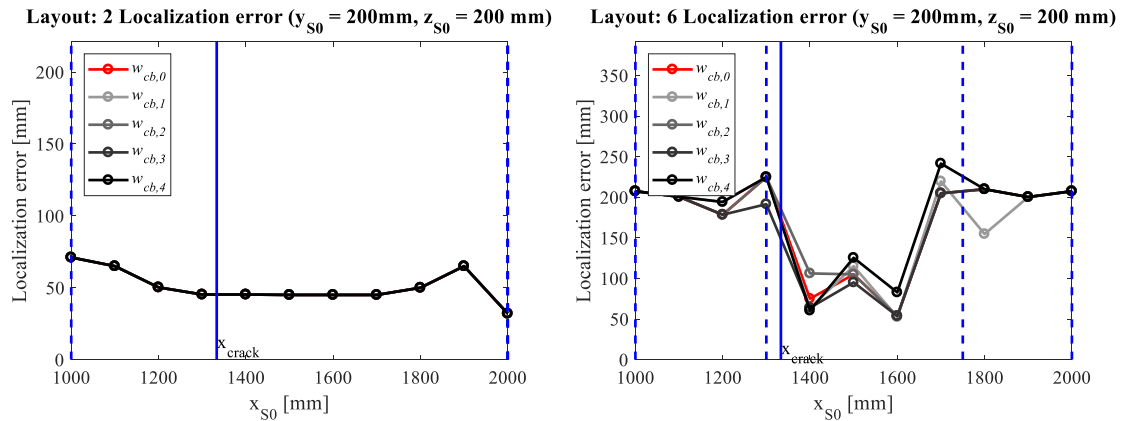


Figure 5.16: Localization errors for sources at neutral line in: (left) layout 2, and (right) layout 6

Maximum localization errors with different crack band tip lengths ( $l_{ct,0}$ ,  $l_{ct,1}$ ,  $l_{ct,2}$ ,  $l_{ct,3}$ ,  $l_{ct,4}$ ) are compared in Figure 5.17. In layout 1, when the tip length was half reduced, the maximum localization error was increased by 50 mm. A graphical comparison between the localization results of using  $l_{ct,0}$  and  $l_{ct,1}$  is made in Figure 5.18. When using  $l_{ct,1}$ , the maximum localization error happened when the source  $S_0$  was at  $x = 1900\text{mm}$ ,  $y = 50\text{mm}$ ,  $z = 300\text{mm}$ , in which case the wave travel path to sensor 2 on top surface was not influenced by the crack band, while the wave travel time to sensor 3 on bottom surface was delayed by the crack. Therefore, the calculated source was located up to the top surface of the detection volume, which made the localization error dominated by z-component. For a same source localization in the condition when crack band was longer, the wave travel paths to the sensors on the top and bottom were both influenced by the crack band, which made the localization error around 100 mm less. It is reasonable that crack length had hardly any influence in 2D layouts and 1D layout, since all the sensors were located at the bottom surface.

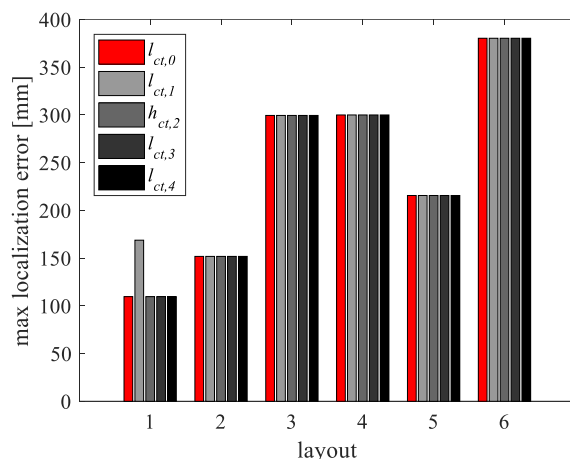


Figure 5.17: Max localization error in each layout with different crack band tip lengths

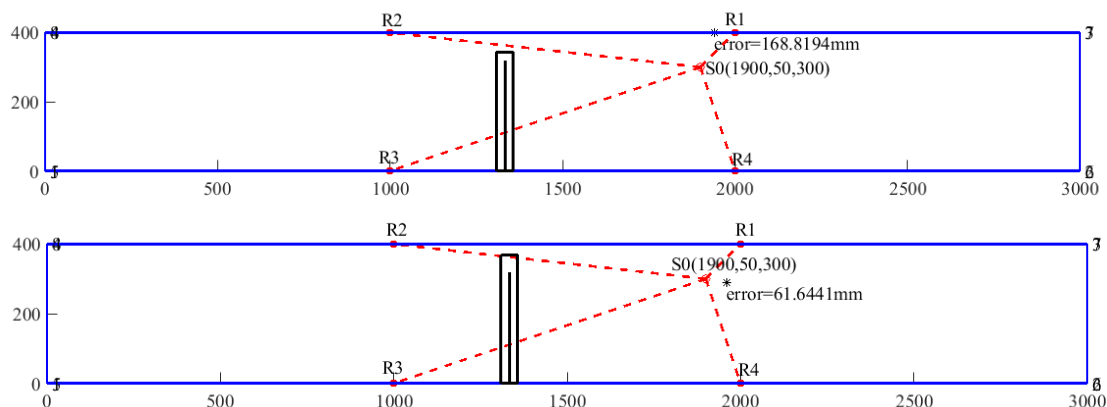


Figure 5.18: Source ( $S_0$ ) localization error in layout 1 with: (top)  $l_{ct,1} = 0.5 \times l_{ct,0}$ , and (bottom)  $l_{ct,0}$

Localization errors for sources in the neutral line were not influenced by tip length in the six layouts. The result of layout 2 is selected as an example and shown in Figure 5.19.

The conclusion is that in 2D and 1D sensor layouts, the crack band size had negligible influence on the localization accuracy, while in 3D sensor layouts, the maximum localization error in the detection volume could decrease when the crack band tip length increased.

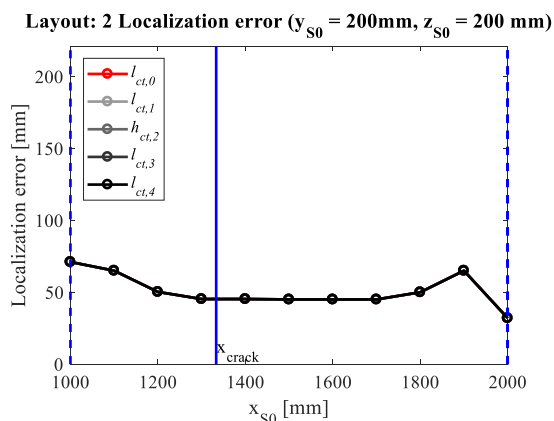


Figure 5.19: Localization errors for sources in the neutral line in layout 2

### 5.3.1.3 Influence of arrival time picking accuracy

A widely-used method for arrival time picking is automatic threshold picking method. In this method, a threshold level is set and the time of the first crossing point is picked as the arrival time. Another picking method is manual picking which requires looking into the shape of the waveform manually. Compared to manual picking, automatic threshold picking method can manage a vast amount of data, but may have larger picking errors, which can influence the localization accuracy. There are two types of automatic threshold picking. One uses a fixed threshold value, and the other one uses float threshold values. By comparing the float-threshold automatic picks and the manual picks in the data acquired in Chapter 4, an picking accuracy of  $\Delta t \leq 5.0\mu s$  was observed. Another research [19] examined the differences between the automatic and the manual picks among 1217 signals of 178 AE events and resulted that 32% of the data had an picking accuracy of  $\Delta t \leq 1.25\mu s$  , 46% had an picking accuracy of  $1.25\mu s \leq \Delta t \leq 2.5\mu s$  , and 22% had an accuracy of  $2.5\mu s \leq \Delta t \leq 5.0\mu s$  . The above literature also showed that the misspicks were more likely in fixed threshold picking method than floating threshold picking method. Based on the observation in the former tests and other research work, influence of arrival time picking accuracy of  $\Delta t \leq 5.0\mu s$  on source localization was studied.

Five hundred uniformly-distributed random arrival time picking errors in range of  $[-5\ 5]\mu s$  were considered for the arrival times of each sensor. The assumptions at the beginning of section 5.3.1 kept same. The probability distribution of the maximum localization errors influenced by the crack and time picking accuracy was a near normal distribution for each layout, shown in Figure 5.20. The filled red circle shows the mean value of the 500 results. The hollow red circle shows the result without the influence of arrival time picking accuracy.

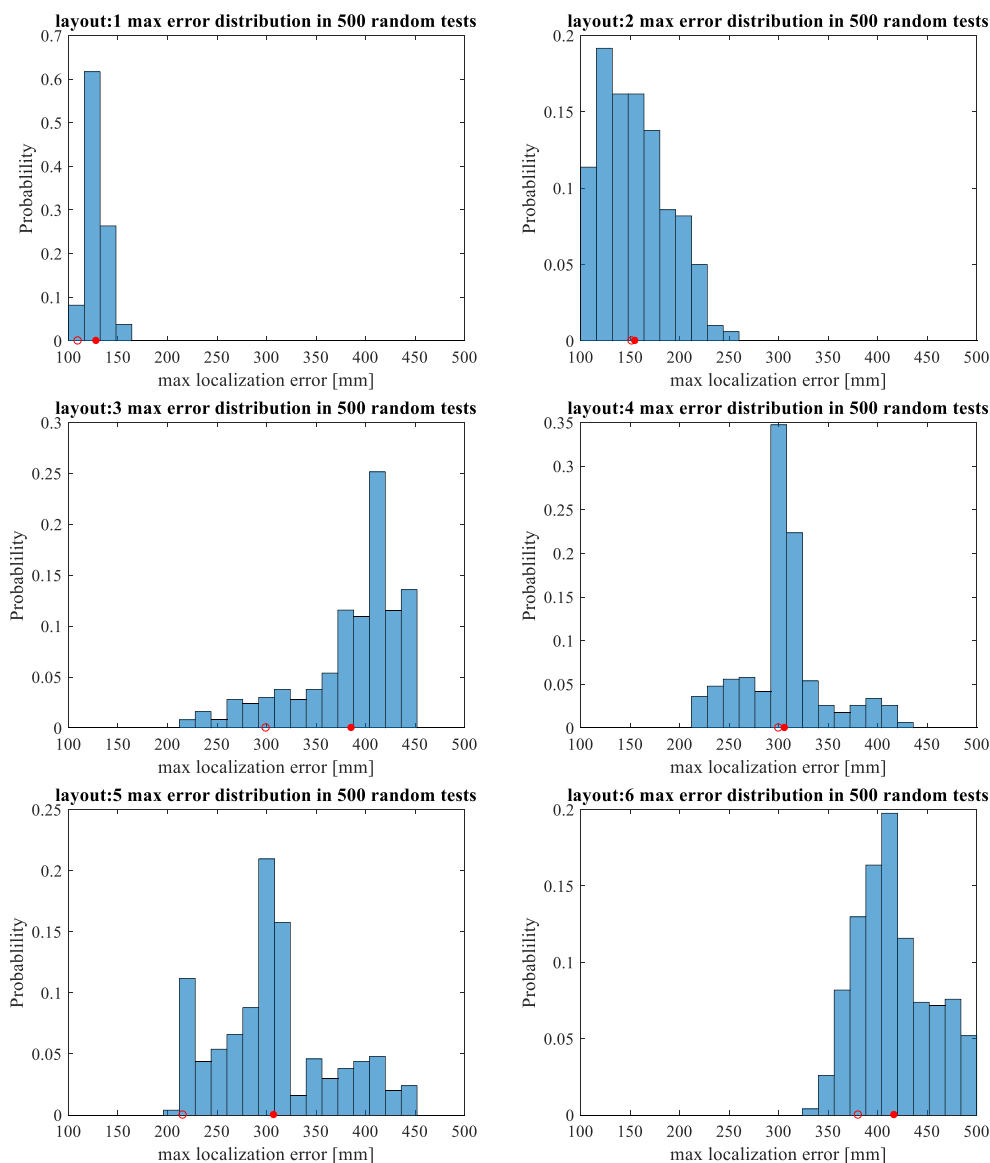


Figure 5.20: Probability distribution of the maximum localization errors with the influence of crack and arrival time picking accuracy

The maximum localization errors with and without the influence of time picking error are compared in Figure 5.21 (left). It can be observed that the influence of time picking accuracy of  $\Delta t \leq 5.0 \mu s$  was less than 20 mm in 3D layouts, which can be neglected. However, the influences in 2D layouts and 1D layouts were larger and could reach 100 mm in layouts 3 and 5. It was expected since some source locations were outside the sensor enclosed area in 2D and 1D layouts. By comparing the maximum localization errors which were inside the sensor enclosed area in Figure 5.21 (right), the influence of time picking accuracy of  $\Delta t \leq 5.0 \mu s$  was limited to 40 mm.

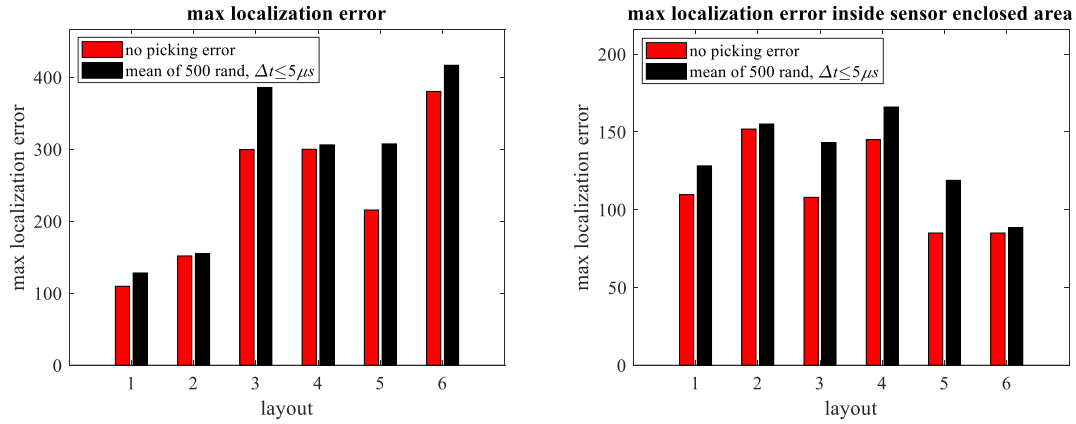


Figure 5.21: Influence of time picking accuracy on: (left) total localization errors and (right) localization errors inside sensor enclosed area

#### 5.3.1.4 Influence of sensor location accuracy

Sensor location uncertainty could probably be caused during installation. An installation error of  $\Delta d \leq 10 \text{ mm}$  was studied. A number of 8 ( $4 \times 2$ ) randomly-generated location errors in range of  $[-10 \ 10] \text{ mm}$  were applied to the two coordinates of the four sensors in the source localization. The assumptions at the beginning of section 5.3.1 kept same. After an iteration of 500 times, the probability distribution of the maximum localization errors can be generated. Figure 5.22 (left) shows the probability distribution in layout 3 as an example. The filled red dot shows the mean value of the 500 results. The hollow red dot shows the result without the influence of arrival time picking accuracy. Figure 5.22 (right) shows a comparison between localization results with and without the influence of sensor location accuracy. It can be concluded that the influence of sensor location accuracy of  $\Delta d \leq 10 \text{ mm}$  was less than 30 mm, which can be neglected.

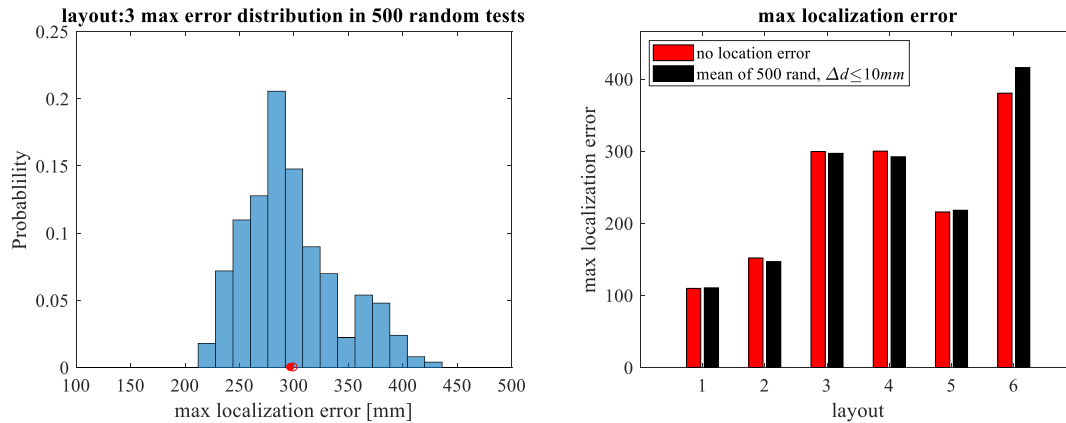


Figure 5.22: Maximum localization errors influenced by crack and sensor location accuracy: (left) in layout 3 and (right) in six layouts

### 5.3.2 Reliability of localization for partially-closed cracks

A partially-closed crack can also influence the reliability of the source localization when the AE signals are attenuated by the crack to a level lower than the acquisition threshold. If some of the sensors fail to receive sufficiently strong signals, the reliability of the AE monitoring will be substantially reduced. From the results of the experiments on the considered beam in Chapter 4, the total attenuation over a 1 m distance, with a narrow crack with 0.05 mm width

would be around 55 dB at a frequency range of [40 100] kHz. Consequently, an AE source with a peak amplitude of 90 dB can only be detected by sensors at 1 m distance if the threshold was 35 dB or smaller. Regarding the noise levels in practice, this can be a very challenging condition, as a result of which many AE events may be missed. Larger crack widths on the surface can naturally have more drastic effects and lead to further-reduced reliability. It is therefore important to include the role of existing cracks when designing AE monitoring systems for existing concrete structures.

### 5.3.3 Accuracy of localization for open cracks

When the cracks become open with acoustically-decoupled faces [21], the crack tip-diffracted waves (shown in section 2.3) may be dominated and picked up upon their exceeding of amplitude threshold. With the assumption of straight wave path, larger arrival time difference may be induced by a fully-opened crack depending on the relative positions of the source, the sensor and the crack tip. The tip-diffracted wave path in the modeling case is shown in Figure 5.23. The gray surface indicates the crack face. The red dash lines are wave travel paths from source to sensors. As can be seen that the wave paths to sensor 1 and sensor 4, which located on the other side of the crack, were diffracted by the crack tip, while the wave paths to sensor 2 and sensor 3 were not influenced by the crack.

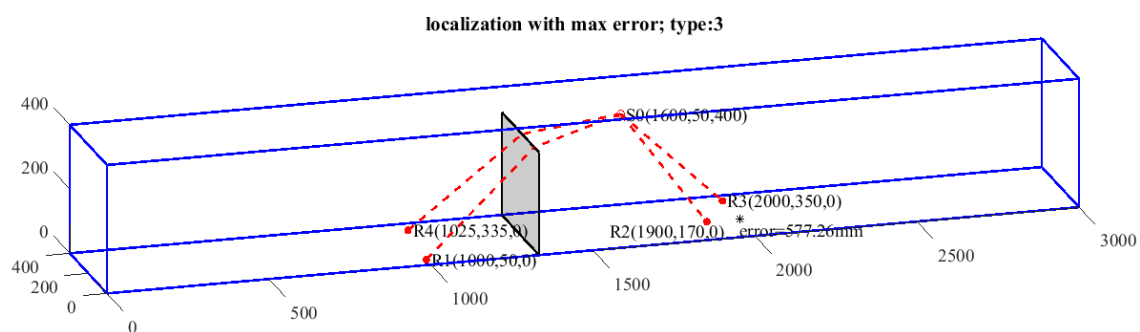


Figure 5.23: Tip-diffracted wave travel path and localization error in layout 3

The localization errors for the 165 selected sources in section 5.2 were calculated and the probability distributions in the six layouts are shown in Figure 5.24. The mean values are indicated by hollow red dot. Compared to the probability distribution of errors in the situation of a partially-closed crack (Figure 5.7), the error distribution in the situation of a fully-open crack was more scattered around a larger mean value. Less difference was observed among different sensor layouts. The influence of layouts on the localization accuracy can be neglected in the case that the crack is fully open.

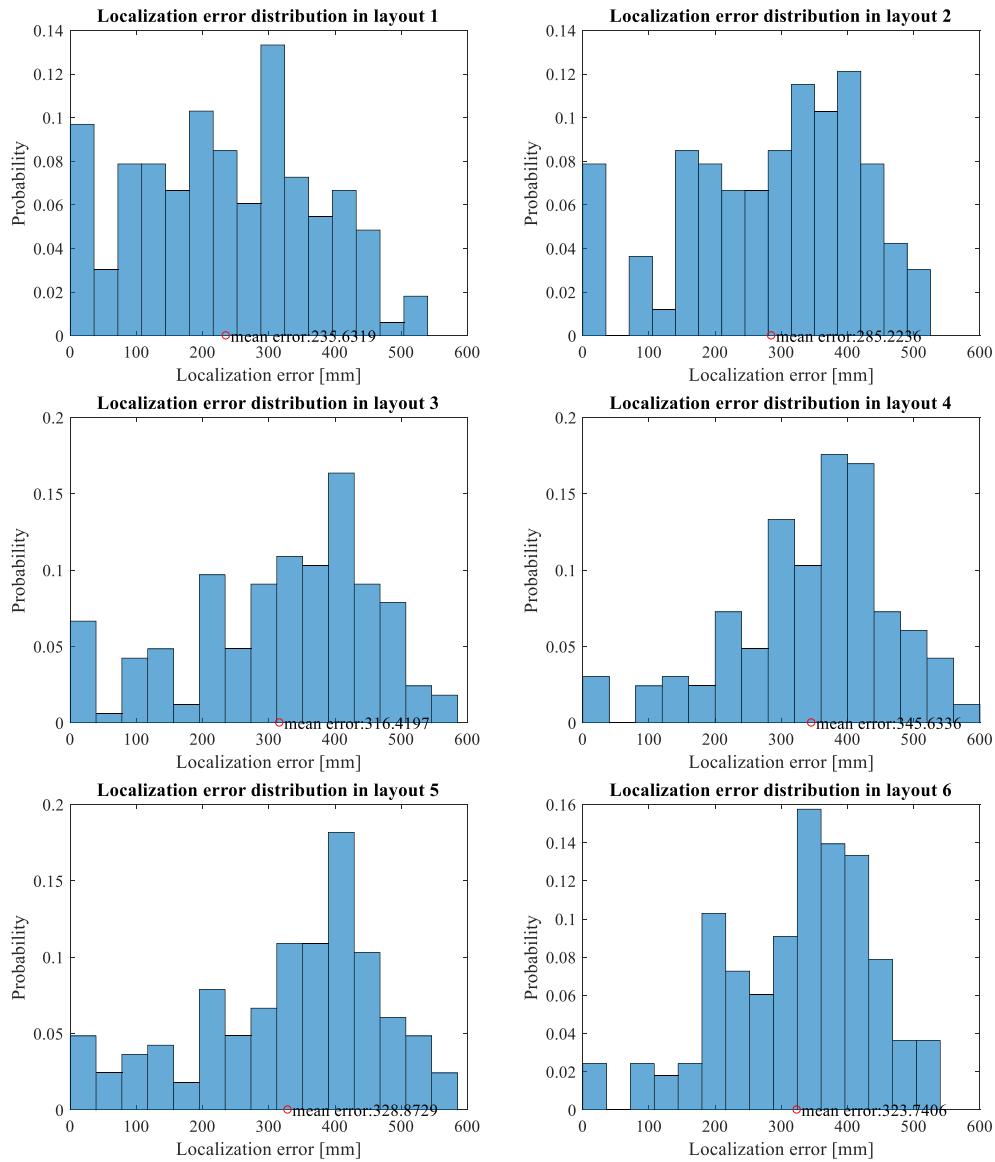


Figure 5.24: Probability distribution of localization errors for 165 sources

The maximum localization error in each layout was picked, as summarized in Figure 5.25 (left). They were around 550 mm without evident difference among different layouts. This error was too inaccurate to estimate the source location in a detection volume of  $1000\text{mm} \times 300\text{mm} \times 400\text{mm}$ . Figure 5.25 (right) shows the mean localization errors, which were around 300 mm.

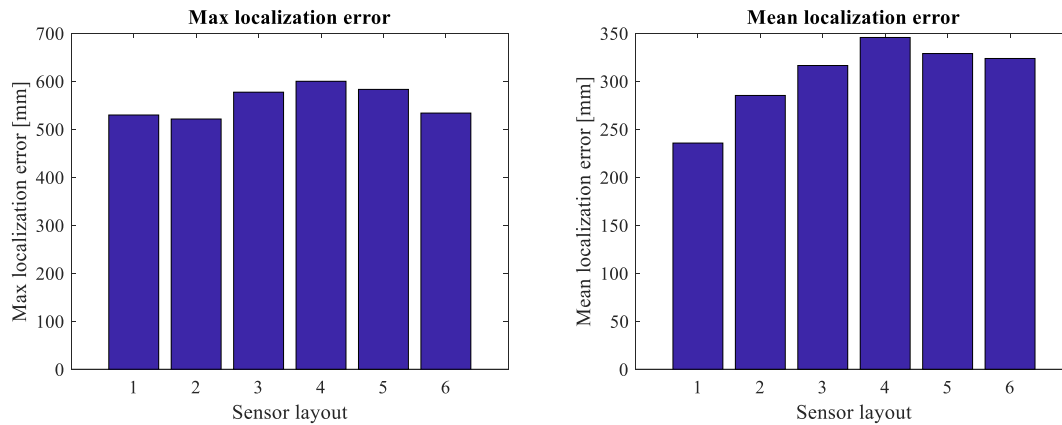


Figure 5.25: (left) maximum localization errors and (right) mean localization errors

### 5.3.4 Reliability of localization for open cracks

In terms of the wave attenuation, over a 1.5-m-long tip-diffracted wave path, for example, the attenuation of the bulk waves was estimated to be less than 65 dB from the conducted measurements in Chapter 4. Assume that the direct wave path from the source to the receiver was 1 m. From the test results in Chapter 4, it can be known that the attenuation over 1 m could be 70 dB when waves travel through a narrow partially-closed crack. The tip-diffracted waves are less attenuated compared to the waves travel through a partially-closed crack. Therefore, the signal diffracted by the tip of the crack has a higher chance to be received, but leads to a less accurate localization result.

## 5.4 Concluding remarks

A crack with height of 320 mm was assumed in a detection volume of 1000mm×300mm×400mm. Analytical studies on the source localization influenced by a partially-closed crack and a fully-opened crack were performed. A number of conclusions are drawn:

- 1) Considering an imperfectly-closed crack, which allowed partial transmission of waves, the maximum localization error for sources inside the sensor coverage area was around 120 mm.
- 2) The sensitivities of localization results to the uncertainties of wave speed distribution in crack area, size of crack area, arrival time picking accuracy and sensor location accuracy were less than 40 mm, which could be neglected.
- 3) In the case that the signal, which was attenuated by a partially-closed, could not be detected, or the crack was fully-open with faces acoustically decoupled, the picked-up signals might be the tip-diffracted waves. It can lead to a larger localization error of around 550 mm.
- 4) In the consideration of the reliability of source localization in the situation of a fully-open crack, the waves may be less attenuated than the waves passing through a partially-closed crack. Therefore, there is a high chance for the tip-diffracted waves to be received.

## 6 Conclusions and recommendations

An investigation of the accuracy and reliability of acoustic emission monitoring of concrete structures in the presence of existing cracks was presented in the previous chapters. The important concluding remarks from this research are reviewed in this chapter. Moreover, some topics which are related to this work but were not fully studied mainly due to the limitation of time are recommended for further research.

### 6.1 Conclusions

A number of main conclusions can be drawn from this research as listed below.

- 1) Based on a simulated wave propagation in a 2D concrete section, the parameter arrival time could be used with some acceptable error. Parameters related to the arrival of the peak amplitude (e.g. counts to peak) and duration time (e.g. counts) could not be used for the study of wave propagation in most cases since they were sensitive to the shape of the waveform (Chapter 3).
- 2) The variance of coupling effect of the viscoelastic adhesive couplant can be limited to 5 dB for a mean value of 85 dB at a frequency around 60 kHz (Chapter 4).
- 3) The speed of the front wave in the tested concrete medium was around 4000 m/s. The material attenuation factor of the specimen was around 20 dB/m at a frequency around 60 kHz. Therefore, the attenuation of body wave and surface wave over 1 m were around 35 dB and 55 dB, respectively (Chapter 4).
- 4) Measurable AE signals can propagate through a partially-closed crack with stable additional travel time of around 20  $\mu$ s. A partially-closed crack may result in the attenuation of AE signals from 55 dB to 85 dB over 1 m. It meant that more cracks may not necessarily lead to recording of more AE activities (Chapter 4).
- 5) Substantial anisotropic property at the crack area was observed. In the direction parallel to the crack, the wave speed was around 80% of the original speed, while in the direction perpendicular to the crack, the wave speed was reduced to around 37% of the original speed (Chapter 4).
- 6) Within the studied situation, the localization error within the area enclosed by sensors is around 120 mm with a partially-closed crack, and is around 550 mm with a fully-open crack. The localization results in an area with a fully-open crack are inaccurate to be used for source localization (Chapter 5).

### 6.2 Recommendations

A number of recommendations can be made for the continuation of this research as listed below:

- 1) For the estimation of the wave attenuation, an assumption of the same material attenuation factor of body wave and surface wave was made. This assumption can be verified by conducting more measurements to study the material attenuation factor of the body wave and surface wave. With this, a more accurate estimation of the reliability of the AE source localization may be obtained.

- 2) The source signals of cracking needs to be accurately studied. More measurements for the characterization of the source property should be carried out.
- 3) In this research, all sensors and transducers were narrowly sensitive at a frequency of around 60 kHz. More investigation on the influence of cracks on the AE signals at other frequencies will be valuable.
- 4) The open crack and the partially-closed crack in this research can be defined more quantified by the loading condition. An investigation of the influence of cracks under different load levels will be valuable.

## A. Appendix: Elastic vector wave equations

Based on the mechanics of a deformed solid, the normal stresses can be expressed as  $\sigma_{xx}, \sigma_{yy}, \sigma_{zz}$ , and the tangential stresses can be expressed as  $\sigma_{xy}, \sigma_{xz}, \sigma_{yz}$ , etc. It is the same with normal strains (i.e.  $\varepsilon_{xx}, \varepsilon_{yy}, \varepsilon_{zz}$ ) and tangential strains (i.e.  $\varepsilon_{xy}, \varepsilon_{xz}, \varepsilon_{yz}$ ). Based on the Hooke's Law, in isotropic solids, the relationship between the elastic stresses and elastic strains can be expressed as:

$$\begin{pmatrix} \varepsilon_{xx} \\ \varepsilon_{yy} \\ \varepsilon_{zz} \end{pmatrix} = \frac{1}{E} \begin{pmatrix} 1 & -\nu & -\nu \\ -\nu & 1 & -\nu \\ -\nu & -\nu & 1 \end{pmatrix} \begin{pmatrix} \sigma_{xx} \\ \sigma_{yy} \\ \sigma_{zz} \end{pmatrix} \quad (\text{A.1})$$

where,  $E$  is the Young's modulus,  $\nu$  is the dynamic Poisson's ratio.

The relationship can be inverted to:

$$\begin{pmatrix} \sigma_{xx} \\ \sigma_{yy} \\ \sigma_{zz} \end{pmatrix} = \begin{pmatrix} \lambda + 2\mu & \lambda & \lambda \\ \lambda & \lambda + 2\mu & \lambda \\ \lambda & \lambda & \lambda + 2\mu \end{pmatrix} \begin{pmatrix} \varepsilon_{xx} \\ \varepsilon_{yy} \\ \varepsilon_{zz} \end{pmatrix} \quad (\text{A.2})$$

$$\begin{pmatrix} \sigma_{xx} \\ \sigma_{yy} \\ \sigma_{zz} \end{pmatrix} = \begin{pmatrix} \lambda + 2\mu & \lambda & \lambda \\ \lambda & \lambda + 2\mu & \lambda \\ \lambda & \lambda & \lambda + 2\mu \end{pmatrix} \begin{pmatrix} \varepsilon_{xx} \\ \varepsilon_{yy} \\ \varepsilon_{zz} \end{pmatrix} \quad (\text{A.3})$$

where,  $\lambda = \frac{\nu E}{(1-2\nu)(1+\nu)}$ ,  $\mu = \frac{E}{2(1+\nu)}$ .

It can be re-written as diagonal matrices:

$$\underline{\underline{\sigma}} = \lambda(\nabla \cdot \underline{\underline{\rho}})\underline{\underline{I}} + 2\mu\underline{\underline{\varepsilon}} \quad (\text{A.4})$$

where,  $\underline{\underline{\rho}}$  is the three dimensional displacement vector:  $\underline{\underline{\rho}} = (\xi, \eta, \varsigma)$ .

Since  $\varepsilon_{xy} = \frac{1}{2} \left( \frac{\partial \eta}{\partial x} + \frac{\partial \xi}{\partial y} \right)$ , Equation (A.4) could be re-written as:

$$\underline{\underline{\sigma}} = \lambda(\nabla \cdot \underline{\underline{\rho}})\underline{\underline{I}} + \mu \left[ \left( \frac{\partial \underline{\underline{\rho}}}{\partial \underline{\underline{r}}} \right) + \left( \frac{\partial \underline{\underline{\rho}}}{\partial \underline{\underline{r}}} \right)^T \right] \quad (\text{A.5})$$

where,  $\underline{\underline{r}} = (x, y, z)$ .

The net force on a cuboid in a stress-field can be expressed as:

$$\frac{\Delta F}{\Delta V} = \nabla \cdot \underline{\underline{\sigma}} \quad (\text{A.6})$$

According to Newton's Law we have:

$$\frac{\Delta F}{\Delta V} = \rho_0 \frac{\partial^2 \underline{\rho}}{\partial t^2} \quad (\text{A.7})$$

where,  $\rho_0$  is the density of the medium.

Therefore, we have:

$$\nabla \cdot \underline{\underline{\sigma}} = \rho_0 \frac{\partial^2 \underline{\rho}}{\partial t^2} \quad (\text{A.8})$$

By combining Equation (A.5) and Equation (A.8), for homogeneous and isotropic elastic media, we can have:

$$\rho_0 \frac{\partial^2 \underline{\rho}}{\partial t^2} = \lambda \nabla \cdot [(\nabla \cdot \underline{\rho}) \underline{I}] + \mu \left[ \nabla \cdot \left( \frac{\partial \underline{\rho}}{\partial \underline{r}} \right) + \nabla \cdot \left( \frac{\partial \underline{\rho}}{\partial \underline{r}} \right)^T \right] \quad (\text{A.9})$$

In the right side of the Equation (A.9):

$$\nabla \cdot [(\nabla \cdot \underline{\rho}) \underline{I}] = \begin{pmatrix} \frac{\partial}{\partial x} & \frac{\partial}{\partial y} & \frac{\partial}{\partial z} \end{pmatrix} \begin{pmatrix} \nabla \cdot \underline{\rho} & 0 & 0 \\ 0 & \nabla \cdot \underline{\rho} & 0 \\ 0 & 0 & \nabla \cdot \underline{\rho} \end{pmatrix} = \nabla (\nabla \cdot \underline{\rho}) \quad (\text{A.10})$$

$$\nabla \cdot \frac{\partial \underline{\rho}}{\partial \underline{r}} = \begin{pmatrix} \frac{\partial}{\partial x} & \frac{\partial}{\partial y} & \frac{\partial}{\partial z} \end{pmatrix} \begin{pmatrix} \frac{\partial \xi}{\partial x} & \frac{\partial \eta}{\partial x} & \frac{\partial \zeta}{\partial x} \\ \frac{\partial \xi}{\partial y} & \frac{\partial \eta}{\partial y} & \frac{\partial \zeta}{\partial y} \\ \frac{\partial \xi}{\partial z} & \frac{\partial \eta}{\partial z} & \frac{\partial \zeta}{\partial z} \end{pmatrix} \quad (\text{A.11})$$

$$= i \left( \frac{\partial^2 \xi}{\partial x^2} + \frac{\partial^2 \xi}{\partial y^2} + \frac{\partial^2 \xi}{\partial z^2} \right) + j \left( \frac{\partial^2 \eta}{\partial x^2} + \frac{\partial^2 \eta}{\partial y^2} + \frac{\partial^2 \eta}{\partial z^2} \right) + k \left( \frac{\partial^2 \zeta}{\partial x^2} + \frac{\partial^2 \zeta}{\partial y^2} + \frac{\partial^2 \zeta}{\partial z^2} \right) = \nabla^2 \underline{\rho}$$

$$\nabla \cdot \left( \frac{\partial \underline{\rho}}{\partial \underline{r}} \right)^T = \begin{pmatrix} \frac{\partial}{\partial x} & \frac{\partial}{\partial y} & \frac{\partial}{\partial z} \end{pmatrix} \begin{pmatrix} \frac{\partial \xi}{\partial x} & \frac{\partial \xi}{\partial y} & \frac{\partial \xi}{\partial z} \\ \frac{\partial \eta}{\partial x} & \frac{\partial \eta}{\partial y} & \frac{\partial \eta}{\partial z} \\ \frac{\partial \zeta}{\partial x} & \frac{\partial \zeta}{\partial y} & \frac{\partial \zeta}{\partial z} \end{pmatrix} \quad (\text{A.12})$$

$$= i \frac{\partial}{\partial x} \left( \frac{\partial \xi}{\partial x} + \frac{\partial \eta}{\partial y} + \frac{\partial \zeta}{\partial z} \right) + j \frac{\partial}{\partial y} \left( \frac{\partial \xi}{\partial x} + \frac{\partial \eta}{\partial y} + \frac{\partial \zeta}{\partial z} \right) + k \frac{\partial}{\partial z} \left( \frac{\partial \xi}{\partial x} + \frac{\partial \eta}{\partial y} + \frac{\partial \zeta}{\partial z} \right) = \nabla (\nabla \cdot \underline{\rho})$$

Therefore, we can the elastic vector wave equation for  $\underline{\rho}(\underline{r}, t)$ :

$$\rho_0 \frac{\partial^2 \underline{\rho}}{\partial t^2} = (\lambda + \mu) \nabla (\nabla \cdot \underline{\rho}) + \mu \nabla^2 \underline{\rho} \quad (\text{A.13})$$

It is known from Helmholtz decomposition [31] that any vector field can be represented as the sum of an irrotational vector field and a divergence-free vector field, which have a scalar potential and a vector potential, respectively.

For irrotational vector field, where  $\nabla \times \underline{\rho} = 0$ , we can get  $\nabla (\nabla \cdot \underline{\rho}) = \nabla^2 \underline{\rho}$  from the identity of  $\nabla \times (\nabla \times \underline{\rho}) \equiv \nabla (\nabla \cdot \underline{\rho}) - \nabla^2 \underline{\rho}$ .

For the wave equation for irrotational fields, we can have:

$$\nabla^2 \underline{\rho} - \frac{1}{\alpha^2} \frac{\partial^2 \underline{\rho}}{\partial t^2} = 0 \quad (\text{A.14})$$

where, the wave propagation velocity is  $\alpha = \sqrt{\frac{\lambda + 2\mu}{\rho_0}} = \sqrt{\frac{E(1-\nu)}{(1-2\nu)(1+\nu)\rho_0}}$ .

The irrotational waves are also called as longitudinal waves, or P-waves.

For the divergence-free waves, the condition of  $\nabla \cdot \underline{\rho} = 0$  is applied to the waves equation. The elastic vector wave equation is then reduced to:

$$\rho_0 \frac{\partial^2 \underline{\rho}}{\partial t^2} = \mu \nabla^2 \underline{\rho} \quad (\text{A.15})$$

The propagation velocity is  $\beta = \sqrt{\frac{\mu}{\rho_0}} = \sqrt{\frac{E}{2(1+\nu)\rho_0}}$ . The divergence-free waves are also called as transverse waves, or S-waves.



## B. Appendix: Geometric spread loss

Before the derivation of geometric spread loss, logarithmic notation: decibels need to be introduced. Huge acoustic values like pressure or power are normally quantified in decibels. The decibel is defined as ten times the base-10 logarithm of the ratio of two powers. The ratio in decibels between two powers  $P_1$  and  $P_2$  can be expressed as:  $10\log\left(\frac{P_1}{P_2}\right)$ . In physics, power is proportional to the square of the pressure. Therefore, the same ratio of the two powers can be expressed as:  $20\log\left(\frac{p_1}{p_2}\right)$ , where  $p_1$  and  $p_2$  are the pressures relate to powers  $P_1$  and  $P_2$ , respectively. Therefore, for quantities similar to power or energy,  $10\log\left(\frac{P_1}{P_2}\right)$  is used, while for quantities similar to pressure,  $20\log\left(\frac{p_1}{p_2}\right)$  is used. Decibel values are used to express geometric spread loss.

Wave propagation is a process that spreads the energy from the source over a larger surface. Because of the conservation of energy, the intensity will decrease when the surface increases. Body waves and surface waves spread in different rules due to different boundary conditions. Body waves follow the rule of spherical spread, while surface waves follow the cylindrical spread rule.

For spherical spread, the sphere surface can be calculated as  $\Sigma = 4\pi r^2$ , where  $r$  is the radius of the sphere, or the travel distance from the source. Assuming two points (1) and (2) with different travel distances of  $r_1$  and  $r_2$ , respectively, the decrease in local intensity is inversely proportional to the ratio of the areas of the sphere surfaces:

$$\frac{I_2}{I_1} = \frac{\Sigma_1}{\Sigma_2} = \frac{4\pi r_1^2}{4\pi r_2^2} = \left(\frac{r_1}{r_2}\right)^2 \quad (\text{B.1})$$

The geometric spread loss of body waves in decibels can be expressed as:

$$SL_b = 10\log\left(\frac{I_2}{I_1}\right) = 20\log\left(\frac{r_1}{r_2}\right) \quad (\text{B.2})$$

For cylindrical spread, the cylinder surface can be calculated as  $\Sigma = 2\pi r \cdot l$ , where  $r$  is the radius of the cylinder, or the travel distance from the source, and  $l$  is the length of the cylinder. The decrease in local intensity between two points (1) and (2) is inversely proportional to the ratio of the spread surfaces:

$$\frac{I_2}{I_1} = \frac{2\pi r_1 \cdot l}{2\pi r_2 \cdot l} = \frac{r_1}{r_2} \quad (\text{B.3})$$

Therefore, the geometric spread loss of surface waves in decibels can be expressed as:

$$SL_s = 10 \log \left( \frac{I_2}{I_1} \right) = 20 \log \left( \sqrt{\frac{r_1}{r_2}} \right) \quad (\text{B.4})$$

As can be seen that the geometric spread loss of body waves is larger than that of surface waves over a same distance.

## Reference

1. Melchers, R.E., *Assessment of Existing Structures--Approaches and Research Needs*. Journal of Structural Engineering, 2001. **127**(4): p. 406-411.
2. Balageas, D., C.-P. Fritzen, and A. Güemes, *Structural health monitoring*. Vol. 90. 2010: John Wiley & Sons.
3. Giurgiutiu, V., A. Zagari, and J. Jing Bao, *Piezoelectric Wafer Embedded Active Sensors for Aging Aircraft Structural Health Monitoring*. Structural Health Monitoring, 2002. **1**(1): p. 41-61.
4. Ihn, J.-B. and F.-K. Chang, *Pitch-catch Active Sensing Methods in Structural Health Monitoring for Aircraft Structures*. Structural Health Monitoring, 2008. **7**(1): p. 5-19.
5. Giurgiutiu, V., *Chapter 1 - Introduction*, in *Structural Health Monitoring with Piezoelectric Wafer Active Sensors (Second Edition)*. 2014, Academic Press: Oxford. p. 1-19.
6. Grosse, C.U. and M. Ohtsu, *Acoustic emission testing: Basics for Research-Applications in Civil Engineering*. 2008. 1-404.
7. Katsaga, T., et al., *Acoustic emission imaging of shear failure in large reinforced concrete structures*. International Journal of Fracture, 2007. **148**(1): p. 29-45.
8. Behnia, A., et al., *Integrated non-destructive assessment of concrete structures under flexure by acoustic emission and travel time tomography*. Construction and Building Materials, 2014. **67, Part B**: p. 202-215.
9. Giurgiutiu, V. and A. Cuc, *Embedded non-destructive evaluation for structural health monitoring, damage detection, and failure prevention*. Shock and Vibration Digest, 2005. **37**(2): p. 83-105.
10. Guyott, C.C., P. Cawley, and R.D. Adams, *The Non-destructive Testing of Adhesively Bonded Structure: A Review*. The Journal of Adhesion, 1986. **20**(2): p. 129-159.
11. Kundu, T., *Acoustic source localization*. Ultrasonics, 2013. **54**: p. 25-38.
12. Carpinteri, A., et al., *Reliable onset time determination and source location of acoustic emissions in concrete structures*. Cement and Concrete Composites, 2012. **34**(4): p. 529-537.
13. Tobias, A., *Acoustic-emission source location in two dimensions by an array of three sensors*. Non-Destructive Testing, 1976. **9**(1): p. 9-12.
14. Ohno, K. and M. Ohtsu, *Crack classification in concrete based on acoustic emission*. Construction and Building Materials, 2010. **24**(12): p. 2339-2346.
15. Ohtsu, M., Y. Kaminaga, and M.C. Munwam, *Experimental and numerical crack analysis of mixed-mode failure in concrete by acoustic emission and boundary element method*. Construction and Building Materials, 1999. **13**(1): p. 57-64.
16. Shiotani, T., et al. *Visualization of damage in RC bridge deck for bullet trains with AE tomography*. in *Springer Proceedings in Physics*. 2015.
17. Shiotani, T., D.G. Aggelis, and O. Makishima, *Global Monitoring of Large Concrete Structures Using Acoustic Emission and Ultrasonic Techniques: Case Study*. Journal of Bridge Engineering, 2009. **14**(3): p. 188-192.
18. Yang, Y., D.A. Hordijk, and A. de Boer. *Acoustic emission measurement in the proof loading of an existing bridge affected by ASR*. in *IALCCE 2016*. 2016. Delft.
19. Schechinger, B. and T. Vogel, *Acoustic emission for monitoring a reinforced concrete beam subject to four-point-bending*. Construction and Building Materials, 2007. **21**(3): p. 483-490.
20. Gollob, S., *Source localization of acoustic emissions using multi-segment paths based on a heterogeneous velocity model in structural concrete*. 2017, ETH Zürich.
21. Tsangouri, E., et al., *Assessment of Acoustic Emission localization accuracy on damaged and healed concrete*. Construction and Building Materials, 2016. **129**: p. 163-171.
22. Fowler, C.M., *The solid earth : an introduction to global geophysics / C. M. R. Fowler*. Vol. 10. 1993.

23. S. Dukhin, A. and P. J. Goetz, *Ultrasound for Characterizing Colloids: Particle Sizing, Zeta Potential, Rheology*. 2002.
24. Freund, L.B., *Dynamic Fracture Mechanics*. Cambridge Monographs on Mechanics. 1990, Cambridge: Cambridge University Press.
25. Ohtsu, M., *Recommendation of RILEM TC 212-ACD: Acoustic emission and related NDE techniques for crack detection and damage evaluation in concrete: Test method for damage qualification of reinforced concrete beams by acoustic emission*. Materials and Structures/Materiaux et Constructions, 2010. **43**(9): p. 1183-1186.
26. Pahlavan, L., et al., *Sensitivity of Ultrasonic Waves to Surface-breaking Cracks in Reinforced Concrete Beams*, in *IIIAE 2016*. 2016: Kyoto.
27. Koekkoek, R.T. and Y. Yang, *Measurement Report on the Transition between Flexural and Shear Failure of RC Beams without Shear Reinforcement*. 2016.
28. Nobile, L., *Micro-damage induced anisotropy in concrete*. Nuclear Engineering and Design, 1995. **156**(1): p. 229-234.
29. Zdenek P. Bazant, B.H.O., *Crack band theory for fracture of concrete*. Materials and Structures 16, 1983: p. 155-177.
30. Koji Otsuka, H.D., *Fracture process zone in concrete tension specimen*. Engineering Fracture Mechanics 65, 2000: p. 111-131.
31. Bladel, J.v., U.S.A.E. Commission, and A. Midwestern Universities Research, *On Helmholtz's theorem in finite regions*. MURA (Series);440. 1958, Madison, Wisconsin: Midwestern Universities Research Association. 32 leaves.





Master Thesis

